



ELSEVIER

Contents lists available at ScienceDirect

## International Journal of Plasticity

journal homepage: [www.elsevier.com/locate/ijplas](http://www.elsevier.com/locate/ijplas)

# Micromechanical crystal plasticity back stress evolution within FCC dislocation substructure

Theodore Zirkle<sup>a,\*</sup>, Ting Zhu<sup>a,b</sup>, David L. McDowell<sup>a,b</sup>

<sup>a</sup> Woodruff School of Mechanical Engineering

<sup>b</sup> School of Materials Science and Engineering, Georgia Institute of Technology, Atlanta, GA 30332

## ABSTRACT

Experiments and theories have suggested the evolution of intragranular back stress is primarily dependent on the characteristics and development of dislocation substructure in face-centered cubic (FCC) metals and alloys. Despite this, continuum modeling of complex cyclic loading phenomena such as inelastic ratchet strain accumulation typically appeals to one of several phenomenological back stress forms with weak connections to physical mechanisms. In the current work, a micromechanically-based back stress evolution law is derived and implemented in a crystal plasticity framework for FCC metals that directly considers the evolution of dislocation substructure. The model is used in a case study of stainless steel 316L (SS316L), and good agreement is found with experiments on single- and poly-crystalline specimens subjected to monotonic, fully-reversed cyclic loading, and stress-controlled cyclic loading with mean stress. Ratcheting is attributed to dislocation substructure formation, dissolution, and stabilization within this physically-based framework.

## 1. Introduction

Continuum constitutive modeling is essential to support engineering applications, and improved computational capabilities have permitted consideration of underlying intragranular structural heterogeneity. Within the context of thermodynamically admissible evolution of internal state variables (ISVs) (Coleman and Gurtin, 1967), rather complex and sophisticated phenomenological constitutive equations have been established to model complex hysteresis behavior under cyclic loading (Chaboche, 2008). Successive generations of such back stress evolution models have been developed that build on the prior generation(s) by adding terms or modifications. Model parameters are typically tuned to available experimental data, with limited predictive capabilities. The present work focuses on building a more predictive approach to back stress evolution in metal plasticity that addresses both the first order Bauschinger effect and second order lack of closure of unloading-reloading response that leads to ratchet strain accumulation under cycling with mean stress. This necessitates modeling of dislocation substructure transients during monotonic and cyclic deformation. The proposed framework strives to rely on parameters that can be computed, e.g., using atomistics or discrete dislocation dynamics, or measured.

The mechanical response of FCC metals and alloys such as SS316L to monotonic and cyclic loading can be characterized by several key phenomena. One of these is the well-known Bauschinger effect (Cottrell, 1953; Milligan et al., 1966) that reveals the presence of long-range directional internal stress (back stress) that develops during loading; upon unloading, the back stress lowers the yield stress in the reverse direction (Mughrabi, 1983). Symmetric strain-controlled loading of initially annealed FCC crystals typically results in cyclic strain hardening, characterized by a stress amplitude that increases with the number of cycles (Kang et al., 2010). The hysteresis loop shape is affected by the back stress evolution. In addition to development of the back stress, cyclic strain hardening is associated

\* Corresponding author

E-mail address: [tzirkle6@gatech.edu](mailto:tzirkle6@gatech.edu) (T. Zirkle).

<https://doi.org/10.1016/j.ijplas.2021.103082>

Received 5 May 2021; Received in revised form 20 July 2021;

Available online 14 August 2021

0749-6419/© 2021 Elsevier Ltd. All rights reserved.

with the accumulation of defects in the material that contribute to non-directional hardening (e.g., threshold stress) (Feltner, 1965). Lastly, we highlight the cyclic accumulation of plastic strain during asymmetric stress-controlled loading in the direction of the mean stress, also known as ratcheting or cyclic creep (Kang et al., 2010). Ratcheting behavior has generally been interpreted as resulting from a lack of closure of hysteresis loops under stress cycling with a mean stress and is commonly modeled using back stress forms that evolve nonlinearly with plastic strain (Armstrong and Frederick, 1966; Ohno and Wang, 1993). This is a kind of second order response. While the underlying origin of the threshold stress is generally well understood as related to accumulation of dislocations and dislocation debris, the lack of appeal to specific physical mechanisms that drive the nuanced nonlinearity of the back stress in models has yet to be fully addressed.

Transmission electron microscopy (TEM) of certain FCC single- and poly-crystals subjected to monotonic and cyclic deformation has established that heterogeneous dislocation patterns form at sufficient levels of straining (Gaudin and Feugas, 2004; Lukáš et al., 1968; Mughrabi, 1987a; Polak, 1991). This so-called dislocation substructure is characterized by relatively dislocation-free regions (channels) surrounded by regions with significantly higher dislocation density (walls) (Mughrabi, 1983). Several works (Mughrabi, 1983, 1987a) proposed the generation of long-range directional internal stresses was due to the presence of the dislocation substructure, suggesting the difference in the short-range non-directional strengths produces different plastic behavior in the two regions. Consequently, the back stress develops in response to plastic incompatibility between the two phases. This theory has been supported by carefully performed experiments. For example, Pham and coworkers (2013) captured TEM images of SS316L subjected to strain-controlled, fully reversed loading and found the back stress could be directly correlated to the degree of substructure development as well as the spatial characteristics of the formed substructure. In a similar fashion, Gaudin and Feugas (2004) investigated the ratcheting behavior of SS316L and proposed that ratcheting rates were driven by the evolution of intragranular strain incompatibilities due to the presence of substructure as well as the dislocation rearrangement and recovery in substructure walls.

Despite Mughrabi's arguments (1983) and experimental observations (Gaudin and Feugas, 2004; Pham et al., 2013), many mesoscopic continuum models rely on back stress models with an unclear micromechanical connection to substructure (Dong et al., 2020; Ren et al., 2020). Two approaches that may be considered are the micromechanical back stress models developed by Sauzay (2008) and Castelluccio and McDowell (2017). These models have utility for fully-reversed loading but are limited in their application to cases of cyclic loading with mean stress. In the current work, we develop a physically-based crystal plasticity model that uses a micromechanical back stress model similar to the form developed by Castelluccio and McDowell (2017) with the important distinction that nonlinearity in the back stress evolution is generated by plastic deformation occurring in the wall phase. The work is organized as follows. First, commonly used back stress forms are briefly reviewed and the justification for their forms discussed. The back stress model form pursued in the current work is then derived. Next, the crystal plasticity model is discussed in detail. Finally, the model is applied in a case study of the uniaxial, room temperature deformation of SS316L subjected to a variety of load histories, including monotonic and cyclic loading.

## 2. Phenomenological back stress forms

One of the most commonly used phenomenological class of models is based on the form introduced by Armstrong and Frederick (AF) (1966). The AF model describes a nonlinear form of kinematic hardening through competition of direct hardening with dynamic recovery. With the bold notation corresponding to the full tensorial representation of a quantity, the rate of the back stress tensor  $\mathbf{B}$  is written for initially isotropic plasticity theory for polycrystals in the form

$$\dot{\mathbf{B}} = C_1 \dot{\epsilon}^p - C_2 \mathbf{B} \dot{p} = C_1 \dot{p} \mathbf{n} - C_2 \mathbf{B} \dot{p} \quad (1)$$

where  $\dot{\epsilon}^p$  is the plastic strain rate tensor and the Euclidian norm of the plastic strain rate tensor is defined by  $\dot{p} = \|\dot{\epsilon}^p\| = \sqrt{\dot{\epsilon}^p : \dot{\epsilon}^p}$ . Quantity  $\mathbf{n} = \dot{\epsilon}^p / \dot{p}$  is the unit normal in the direction of the plastic strain rate,  $C_1$  is the direct hardening coefficient, and  $C_2$  is an additional dynamic recovery coefficient. The dynamic recovery term is collinear with  $\mathbf{B}$  and scales with the norm of the plastic strain rate  $\dot{p}$ . Prager's classical model (Prager, 1956) is given by the first term only (e.g.,  $C_2 = 0$ ) and corresponds to a linear kinematic hardening form. The AF model is known to overestimate the severity of ratchet strain accumulation while Prager's model is unable to capture ratchet strain accumulation at all for stress-controlled cycling with mean stress (McDowell, 1995; Ohno and Wang, 1993). Chaboche proposed an additive superposition of  $M$  kinematic hardening variables, i.e.,  $\dot{\mathbf{B}} = \sum_{i=1}^M \dot{\mathbf{B}}_i$  (Chaboche et al., 1979), to better fit the elastic-plastic transition after initial yield; however, this modification alone does not substantially improve the description of ratcheting behavior.

Several variations of the AF model have been introduced expressly to better model lack of closure of unloading-reloading hysteresis response and associated ratcheting rate for cycling under mean stress. Ohno and Wang (OW) (1993) introduced a modification of the dynamic recovery term to introduce additional nonlinearity to limit the rate of ratcheting, i.e.,

$$\dot{\mathbf{B}} = C_1 \dot{\epsilon}^p - C_2 \left( \frac{\|\mathbf{B}\|}{C_1/C_2} \right)^m \mathbf{B} \left\langle \mathbf{n} : \frac{\mathbf{B}}{\|\mathbf{B}\|} \right\rangle \dot{p} \quad (2)$$

where  $\|\mathbf{B}\| = \sqrt{\mathbf{B} : \mathbf{B}}$ . Here,  $m$  ( $0 \leq m \leq \infty$ ) is a parameter that controls the degree of nonlinearity as  $\|\mathbf{B}\|$  approaches the saturation limit  $C_1/C_2$ . In the dynamic recovery term of the OW model, the value of  $m$  is used to reduce the rate of ratcheting to agree more closely with experiments. For small values of  $m$ , the nonlinear behavior of the AF model is recovered. Alternatively, large values of  $m$  exhibit linear behavior aligning with Prager's model prior to the nonlinear approach to saturation of the back stress. Additional studies have

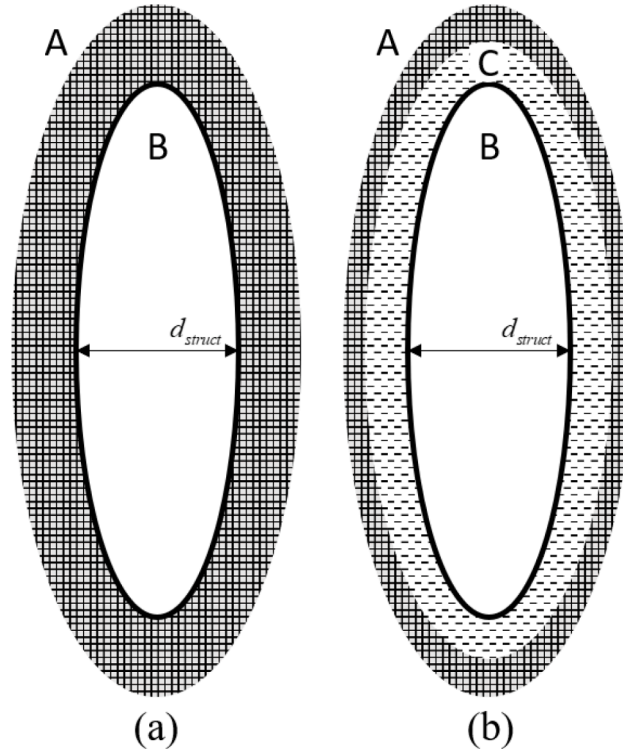


**Fig. 1.** (a) Schematic of an orthogonal projection of a single dislocation channel, assumed periodic, considering a slip system for which an elastoplastic channel phase B is surrounded by an elastic wall phase A. This is the dislocation substructure approximation assumed by prior approaches that derive micromechanical descriptions of the channel phase back stress (Castelluccio and McDowell, 2017; Sauzay, 2008). (b) The same projection of a slip system for which an elastoplastic channel phase B is surrounded by an elastoplastic wall phase composed of mobile wall dislocations (dashed, C) and a substantially less mobile wall dislocation core region (hatched, A).

proposed further modifications, leveraging the general form shown in Eq. (2), and the model of Jiang and Sehitoglu (1996) is mentioned in this regard. Note that Eq. (2) can also employ a multi-component framework, i.e.,  $\mathbf{B} = \sum_{i=1}^M \mathbf{B}_i$ . The AF and OW models are often implemented using multiple components of back stress (McDowell, 2008; Moosbrugger and McDowell, 1989), further increasing the number of phenomenological fitting constants required.

### 3. Model development

#### 3.1. Micromechanical back stress derivation

As discussed by Castelluccio and McDowell (2017), shifting focus from phenomenological forms to physically-based equations i) limits the number of parameters that must be fit using experiments and ii) facilitates enhanced understanding of the role of underlying physical processes. Such physically-motivated constitutive frameworks attempt to directly leverage known physical constants as well as micromechanical parameters of unit processes based on lower length scale simulations (Kubin et al., 2008; Sauzay, 2008; Sauzay et al., 2014; Steckmeyer et al., 2012).

The remainder of this work focuses on intragranular back stress evolution associated with dislocation substructure in crystal plasticity. The isotropic strengthening component, denoted by  $S$ , is commonly considered in crystal plasticity frameworks that explicitly evolve dislocation density  $\rho$  by using the so-called Taylor hardening relation (Kocks and Mecking, 2003), i.e.,

$$S = \mu b \sqrt{A \rho} \quad (3)$$

where  $\mu$  is the shear modulus,  $b$  is the magnitude of the Burgers vector, and  $A$  is a coefficient that describes the interaction strength between dislocations. Continuum models that consider dislocation density evolution seek to incorporate key aspects of dislocation multiplication, annihilation, and cross slip into the constitutive framework (Arsenlis and Parks, 2002; Bayerschen et al., 2016; Castelluccio and McDowell, 2017; Essmann and Mughrabi, 1979; Patra and McDowell, 2012).

Many continuum models that attempt to relate back stress evolution to physically observed phenomenon still rely on kinematic hardening functional forms with unclear micromechanical origins. For example, certain dislocation density based crystal plasticity models (Dong et al., 2020; Dong et al., 2014) explicitly model the evolution of dislocation density to develop the isotropic hardening

variable, but still rely on the AF model form and parameterizable constants to evolve the back stress. Similarly, the crystal plasticity model developed by Ren et al. (2020) tracks the density of multiple dislocation populations, but still only uses the varying dislocation populations to scale the pre-multipliers in a phenomenological nonlinear back stress form.

In contrast, the back stress models developed by Sauzay (2008) and Castelluccio and McDowell (2017) are formulated based on a micromechanical approach that considers the influence of dislocation substructure. Both of these models consider the continuum to be composed of an elastoplastic phase (channels) enclosed by an elastic phase (walls). This interpretation of the dislocation substructure is presented in Fig. 1(a). In this schematic, a top-down view of a slip plane is shown where a single elastoplastic channel phase (denoted by label B) is surrounded by an elastic wall phase (denoted by label A). Note that the periodic nature of the substructure is omitted for clarity. Following prior work that leverages Eshelby’s ellipsoidal inclusion analysis (Eshelby, 1957; Mura, 2013), the back stress evolution in the elastoplastic channel phase on a specific slip system  $\alpha$  takes the form

$$\dot{B}_c^\alpha = \frac{f_w}{1 - f_w} f(\eta, f_{accom}^\alpha) \dot{\gamma}_p^\alpha \tag{4}$$

where  $f(\eta, f_{accom}^\alpha)$  is a function derived using Eshelby’s inclusion analysis that depends on the shape of the channel phase,  $\eta$ , and the degree of plastic accommodation at the interface of the two phases,  $f_{accom}^\alpha$ . Eq. (4) also depends on the volume fraction of the elastic phase, denoted by  $f_w$ , i.e., the volume fraction of dislocation-dense walls. Finally, Eq. (4) shows that in this model framework, the back stress on slip system  $\alpha$  is driven by the plastic shearing rate on slip system  $\alpha$ , denoted  $\dot{\gamma}_p^\alpha$ . Factor  $f_{accom}^\alpha$  is defined as the instantaneous plastic deformation tangent at the slip system level, i.e.,  $f_{accom}^\alpha = \frac{1}{2} \frac{d\gamma_p^\alpha}{d\epsilon^\alpha}$ .

If one considers a sufficiently slow rate of substructure evolution such that  $f_w$  and  $\eta$  can be considered constant on a cycle-by-cycle basis, as done by Castelluccio and McDowell (2017), the back stress evolution form at the slip system level presented in Eq. (4) can be recognized as a linear or direct hardening form, akin to Prager’s linear kinematic hardening. Castelluccio and McDowell (2017) applied Eq. (4) in a crystal plasticity framework to model symmetric, strain-controlled cyclic loading with the goal of modeling the stress-strain response and corresponding substructure at relatively high cycle counts. By using the back stress form shown in Eq. (4) and adopting approximate expressions describing substructure development, Castelluccio and McDowell (2017) were able to obtain good agreement with experimental stress-strain responses. However, linear kinematic hardening forms are ill-equipped to capture cyclic strain ratcheting responses under cycling with mean stress.

In the following, we take a similar approach to Sauzay (2008) and Castelluccio and McDowell (2017) but relax the assumption of purely elastic deformation occurring in the wall phase. Relaxation of this assumption corresponds to the consideration of a more general case where plastic deformation is able to occur in either phase. Specifically, we adopt a dislocation substructure interpretation similar to Hasegawa et al. (1986). This dislocation substructure treatment is shown in Fig. 1(b). In this schematic, a top-down view of a slip plane is shown where an elastoplastic channel phase (denoted by label B) is surrounded by an elastoplastic wall phase comprised of loosely-tangled, mobile wall dislocations (dashed, C) and a tightly-tangled, substantially less mobile wall dislocation core (hatched, A). Using this qualitative interpretation as a guide, we start from Hill’s differential approach (1965) and following Berveiller and Zaoui (1978), write

$$\dot{\sigma}_c = \dot{\hat{\sigma}} + \mathbf{L}'(\mathbf{S}^{-1} - \mathbf{I}) \left( \dot{\hat{\epsilon}} - \dot{\epsilon}_c \right) \tag{5}$$

where  $\dot{\sigma}_c$  and  $\dot{\epsilon}_c$  are the stress and strain rates in the channel phase, considered to be an analog for an Eshelby inclusion, and  $\dot{\hat{\sigma}}$  and  $\dot{\hat{\epsilon}}$  are the stress and strain rates for the effective medium.  $\mathbf{L}'$  and  $\mathbf{S}$  are the constraint and Eshelby tensors, respectively. By decomposing the strain into elastic and plastic components and assuming linear elasticity with a stiffness tensor  $\mathbf{C}$  (Khan and Huang, 1995), Eq. (5) can be rewritten as

$$[\mathbf{I} + \mathbf{L}'(\mathbf{S}^{-1} - \mathbf{I})\mathbf{C}^{-1}] \left( \dot{\sigma}_c - \dot{\hat{\sigma}} \right) = \mathbf{L}'(\mathbf{S}^{-1} - \mathbf{I}) \left( \dot{\hat{\epsilon}}^p - \dot{\epsilon}_c^p \right) \tag{6}$$

where the superscript  $p$  corresponds to plastic behavior and  $\mathbf{I}$  corresponds to the rank four identity tensor. At this point, the expression in Eq. (6) can be simplified for use in a crystal plasticity context by making some assumptions regarding loading mode and channel shape. Due to the complexity of the Eshelby solution, closed-form solutions exist for only a limited number of geometries. Following Castelluccio and McDowell (2017), we assume a prolate spheroid channel phase undergoing pure shear. While other shapes can be assumed, the current work is more focused on exploration of the driving force for back stress development, and investigation of alternate channel phase shapes is left to future work. In this case, the prolate spheroid shape and size are respectively defined by two quantities,  $\eta$  and  $d_{struct}$ . Here,  $\eta$  defines the ratio of major to minor axis lengths while  $d_{struct}$  approximately defines the length of the minor axes. For large values of  $\eta$ , the prolate spheroid resembles a dislocation free channel associated with vein or PSB-type substructures. Conversely, for  $\eta \approx 1$  the prolate spheroid resembles a sphere and can be considered to approximate equiaxed cell substructures. By assuming that the channel structures can be approximated as a prolate spheroid with some aspect ratio  $\eta$  subjected to pure shear (Eshelby, 1957; Mura, 2013), Eq. (6) can be applied to a specific slip system  $\alpha$  as

$$\dot{\tau}_c^\alpha - \dot{\hat{\tau}}^\alpha = \frac{2\mu_m^\alpha \frac{1-2S_{1212}^\alpha}{2S_{1212}^\alpha}}{1 + \frac{\mu_m^\alpha}{\mu} \frac{1-2S_{1212}^\alpha}{2S_{1212}^\alpha}} \left( \dot{\gamma}_p^\alpha - \dot{\gamma}_{p,c}^\alpha \right) \tag{7}$$

where the  $\tau^\alpha$  values denote resolved shear stresses and the  $\dot{\gamma}_p^\alpha$  values denote plastic shearing rates, both evaluated for slip system  $\alpha$ . Again, the subscript  $c$  denotes the channel phase and the overhat  $\hat{\cdot}$  corresponds to the effective medium. In Eq. (7), the quotient on the right takes into account the channel aspect ratio  $\eta$  and the accommodation of the interface between channel and wall phases through a component of the Eshelby tensor,  $S_{1212}^\alpha$ , and modified shear modulus,  $\mu_m^\alpha$ ;  $S_{1212}^\alpha$  is defined using a shape factor,  $K_{shape}$ , and modified Poisson's ratio,  $\nu_p^\alpha$ , as (Mura, 2013)

$$S_{1212}^\alpha = \frac{\pi\eta^2 + (\eta^2 - 1.75 - 2\nu_p^\alpha\eta^2 + \nu_p^\alpha)K_{shape}}{8\pi(1 - \nu_p^\alpha)(\eta^2 - 1)} \tag{8}$$

$$K_{shape} = \frac{2\pi\eta(\eta\sqrt{(\eta^2 - 1)} - \cosh^{-1}(\eta))}{\sqrt{(\eta^2 - 1)^3}} \tag{9}$$

$$\nu_p^\alpha = \frac{\nu + 2/3\mu(1 + \nu)f_{accom}^\alpha}{1 + 4/3\mu(1 + \nu)f_{accom}^\alpha} \tag{10}$$

The quantity  $\mu_m^\alpha$  is defined (Berveiller and Zaoui, 1978) as

$$\mu_m^\alpha = \frac{\mu}{1 + 2\mu f_{accom}^\alpha} \tag{11}$$

For sake of presentation efficiency, we replace the quotient on the right in Eq. (7) with  $f(\eta, f_{accom}^\alpha)$  as done in Eq. (4). Doing so yields the more manageable expression

$$\hat{\tau}_c^\alpha - \hat{\tau}^\alpha = f(\eta, f_{accom}^\alpha) (\hat{\gamma}_p^\alpha - \dot{\gamma}_{p,c}^\alpha) \tag{12}$$

Following Castelluccio and McDowell (2017), we consider the plastic shearing rate over the effective medium to have contributions from the plastic shear strain rate of the wall and channel phases, proportional to their respective volume fractions, i.e.,

$$\hat{\gamma}_p^\alpha = f_w \dot{\gamma}_{p,w}^\alpha + f_c \dot{\gamma}_{p,c}^\alpha \tag{13}$$

where the  $w$  subscript corresponds to the wall phase and the  $c$  subscript corresponds to the channel phase as before. By assuming that the channel and wall phases comprise the entire effective volume, i.e.,  $f_c + f_w = 1$ , Eq. (13) can be simplified as

$$\hat{\gamma}_p^\alpha = f_w \dot{\gamma}_{p,w}^\alpha + (1 - f_w) \dot{\gamma}_{p,c}^\alpha \tag{14}$$

By combining Eqs. (12) and (14) and recognizing that the difference between the stress rate on the effective medium and the stress rate in the channel phase corresponds to the back stress, the final expression for the channel phase back stress evolution rate on slip system  $\alpha$  is derived as

$$\dot{B}_c^\alpha = f_w f(\eta, f_{accom}^\alpha) (\dot{\gamma}_{p,c}^\alpha - \dot{\gamma}_{p,w}^\alpha) \tag{15}$$

Here, we note that assuming a different channel phase shape would only modify the term  $f(\eta, f_{accom}^\alpha)$ , and the general form shown in Eq. (15) is invariant to assumed channel phase shape. Comparing Eqs. (4) and (15), we see that by allowing plastic deformation in the wall phase, we modify the driving force for back stress evolution. In Eq. (4), the back stress in the channel phase is driven by the plastic shearing rate,  $\dot{\gamma}_p^\alpha$ , whereas in Eq. (15), the back stress is driven by the difference in the channel and wall plastic shearing rates,  $\dot{\gamma}_{p,c}^\alpha - \dot{\gamma}_{p,w}^\alpha$ . Considering that the back stress is self-equilibrated (Mughrabi, 1983), the net back stress rate vanishes, i.e.,  $(1 - f_w)\dot{B}_c^\alpha + f_w\dot{B}_w^\alpha = 0$ . The corresponding directional stress in the wall phase is

$$\dot{B}_w^\alpha = -\frac{1 - f_w}{f_w} \dot{B}_c^\alpha \tag{16}$$

where it is clear that the directional internal stress in the walls acts in the opposite direction to that in the channels.

The back stress model described by Eqs. (15) and (16) depends on the slip system shearing rates in both the channel and wall phases. In this approach, nonlinear back stress evolution arises naturally as a consequence of Eqs. (15) and (16), as well as from distinct strengths in the channel and wall phases. This is useful in avoiding a high degree of phenomenology.

### 3.2. Crystal plasticity model

The viability of the slip system level back stress form derived in Eq. (15) was studied through implementation in a crystal plasticity model for SS316L. The crystal plasticity model uses many elements of the microstructure sensitive crystal plasticity model developed by Castelluccio and McDowell (2017) for substructure development in fully reversed loading, but is modified to consider plastic

deformation in both channel and wall phases. The goal of the current model is to describe stress-strain behavior exhibited from several to tens of cycles for both fully reversed loading and stress-controlled cycling with mean stress. First, the flow rule will be established. Next, the evolution of dislocation densities will be defined. The formulations describing substructure evolution are then presented, followed by parameter estimates for SS316L at room temperature.

### 3.3. Flow rule

To implement the back stress evolution equation proposed in Eq. (15), we extend the previous crystal plasticity framework to consider both  $\dot{\gamma}_{p,c}^\alpha$  and  $\dot{\gamma}_{p,w}^\alpha$ . To do so, some assumptions must be made regarding the kinematic behavior of the composite structure of walls and channels. First, the deformation gradient is assumed to be the same for channels and walls, akin to the assumption of compatibility of deformation in Mughrabi's treatment (1983). Furthermore, we consider the plastic shearing rate over the effective medium to have contributions from the shearing rates in the walls and channels, consistent with Eq. (13).

The standard crystal plasticity model expresses the plastic velocity gradient in terms of the slip system shearing rates, i.e.,

$$L^p = \sum_{\alpha=1}^{12} \dot{\gamma}_p^\alpha s_0^\alpha \otimes m_0^\alpha \tag{17}$$

where  $s_0^\alpha$  and  $m_0^\alpha$  are the slip direction and slip plane normal unit vectors for slip system  $\alpha$  in the isoclinic intermediate configuration (same as in the reference configuration). In the current framework, Eq. (14) is used with Eq. (17) to define  $L^p$ , i.e.,

$$L^p = \sum_{\alpha=1}^{12} \left[ (1 - f_w) \dot{\gamma}_{p,c}^\alpha + f_w \dot{\gamma}_{p,w}^\alpha \right] \left[ s_0^\alpha \otimes m_0^\alpha \right]. \tag{18}$$

The slip system shearing rates obey the model forms described by Asaro (1983) for both channel and wall phases. We assume that the plastic deformation is rate-limited by the dislocation bypass of short range obstacles as described by the Kocks-Argon-Ashby (1975) thermally activated flow rule, i.e.,

$$\dot{\gamma}_{p,c}^\alpha = \dot{\gamma}_{c,0}^\alpha \exp \left[ - \frac{F_0}{k_B T} \left( 1 - \left[ \frac{\tau_{c,eff}^\alpha}{s_0 \frac{\mu}{\mu_{@0K}}} \right]^p \right)^q \right] \text{sgn}(\tau^\alpha - B_c^\alpha) \tag{19}$$

$$\dot{\gamma}_{p,w}^\alpha = \dot{\gamma}_{w,0}^\alpha \exp \left[ - \frac{F_0}{k_B T} \left( 1 - \left[ \frac{\tau_{w,eff}^\alpha}{s_0 \frac{\mu}{\mu_{@0K}}} \right]^p \right)^q \right] \text{sgn} \left( \tau^\alpha + \frac{1 - f_w}{f_w} B_c^\alpha \right) \tag{20}$$

where  $\dot{\gamma}_{c,0}^\alpha$  and  $\dot{\gamma}_{w,0}^\alpha$  are reference shearing rates,  $\tau_{c,eff}^\alpha$  and  $\tau_{w,eff}^\alpha$  are the effective stresses driving dislocation bypass,  $F_0$  is the activation energy for short range dislocation barrier bypass,  $k_B$  is the Boltzmann constant,  $T$  is the absolute temperature,  $s_0$  is the thermal slip resistance at 0 K, and  $\mu_{@0K}$  is the shear modulus at 0 K. Note that we use Eq. (16) to express  $B_w^\alpha$  in terms of  $B_c^\alpha$  in Eq. (20). Strictly speaking,  $F_0$  may differ between wall and channel phases upon sufficient dislocation densification in the wall phase acknowledging potentially different dislocation reactions. However, lacking details of such distinction, we treat  $F_0$  as the same for both phases and model the hardening in the wall phase through the evolution of dislocation density using a Taylor-type relation (Taylor, 1934).

The reference shearing rates follow the argument of Kocks et al. (1975). The channel phase reference shearing rate is written as

$$\dot{\gamma}_{c,0}^\alpha = \rho_c^\alpha l_c b v_G \tag{21}$$

where  $\rho_c^\alpha$  is the mobile dislocation density in the channel phase,  $l_c$  is the mean glide distance for dislocations in the channel phase, and  $v_G$  is an estimate of the bypass attempt frequency (Langer et al., 2010). Similarly, the wall phase reference shearing rate is written as

$$\dot{\gamma}_{w,0}^\alpha = \rho_{w,m}^\alpha l_w b v_G \tag{22}$$

where  $\rho_{w,m}^\alpha$  is the mobile dislocation density component of the total wall dislocation density  $\rho_w^\alpha$  and  $l_w$  is the mean glide distance for mobile dislocations in the wall phase. The decomposition of the total wall dislocation density into mobile and immobile components will be discussed in a subsequent section.

The effective stresses driving thermally-activated dislocation bypass of barriers account for scalar threshold and directional back stresses (Chaboche, 2008; Mughrabi, 1983). The effective stresses in the channel and wall phases are written as

$$\tau_{c,eff}^\alpha = \langle |\tau^\alpha - B_c^\alpha| - S_c^\alpha \rangle \tag{23}$$

$$\tau_{w,eff}^\alpha = \left\langle \left| \tau^\alpha + \frac{1 - f_w}{f_w} B_c^\alpha \right| - S_w^\alpha \right\rangle \tag{24}$$

where  $\tau^\alpha$  is the resolved shear stress and again we use Eq. (16) to express  $B_w^\alpha$  in terms of  $B_c^\alpha$ . The  $\langle \rangle$  denote Macaulay brackets, i.e.,  $\langle$

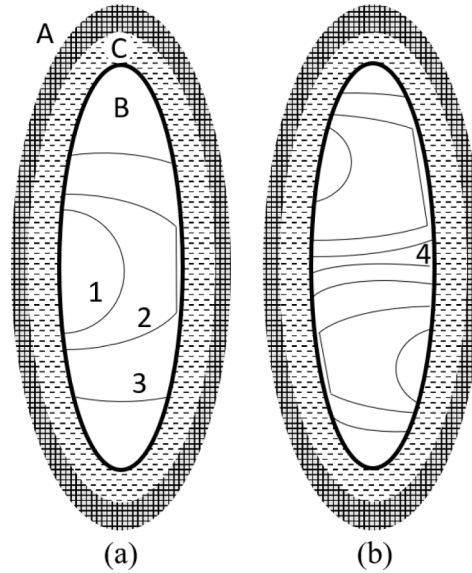


**Fig. 2.** Schematic of orthogonal projection of dislocation substructure showing several dislocation bow-out processes in a single channel/wall unit. (a) Point 1 shows a dislocation bow-out event from the wall phase. Point 2 is reached when the dislocation strikes the adjacent wall, depositing an edge dislocation segment in the wall and generating screw dislocation segments that span the channel. At point 3, the resulting screw dislocation segments traverse the length of the dislocation channel phase and produce shear strain. (b) Upon reaching the configuration shown at Point 4, opposing dislocation pile-ups are observed within the same structure. The meaning of A, B, and C labels are provided in Fig. 2.

$g) = 0$  if  $g \leq 0$  and  $\langle g \rangle = g$  if  $g > 0$ . Note the distinction of the threshold stresses in the channels ( $S_c^\alpha$ ) and in the walls ( $S_w^\alpha$ ).

### 3.4. Threshold stress

In accordance with experiments, we assume that threshold stress hardens with the accumulation of dislocations and can be described using a Taylor-type relation similar to the one presented in Eq. (3) (Kubin et al., 2008). Accordingly,  $S_c^\alpha$  is defined as

$$S_c^\alpha = \mu b \sqrt{A_{aa} \rho_c^\alpha} \quad (25)$$

where  $A_{aa}$  corresponds to the self-interaction coefficient as a subset of the full  $12 \times 12$  interaction matrix  $A_{a\zeta}$  (Gérard et al., 2013; Kubin et al., 2008; Schwartz et al., 2013). In the definition of  $S_c^\alpha$ , only the self-interaction of dislocations is accounted for, essentially corresponding to two opposing pile-ups developing within the same substructure unit (Castelluccio and McDowell, 2017), shown schematically in Fig. 2(b). In this schematic, dislocation pile-ups with the same sign meet in the center of the channel structure at the location denoted by “4”, generating self-interactions consistent with the  $A_{aa}$  component of the full interaction matrix. Neglect of interactions of dislocations on different slip systems is consistent with experimental evidence that the channel phase has a relatively low dislocation density and is largely absent of dislocation locks (Conti and Ortiz, 2005; Feugas, 1999; Hansen et al., 2010). Consideration of the full interaction matrix in the channel phase overestimates the degree of hardening when compared with macroscopic stress-strain curves for nickel (Castelluccio and McDowell, 2017).

On the other hand, the dislocation density in the walls is higher than in the channels (Feugas, 1999; Mughrabi, 1983), and the interactions of dislocations on different slip systems cannot be ignored. While we assume that edge dislocation components are deposited in the wall phase (as will be discussed shortly), the dislocation tangles formed within the wall phase from previously deposited edge dislocation components tend to stack on top of each other in order to relax the stresses associated with concave-loop groups (Hasegawa et al., 1986; Kocks, 1966). Non-planar interactions need to be considered and accordingly,  $S_w^\alpha$  is defined as

$$S_w^\alpha = \mu b \sqrt{\sum_{\zeta=1}^{12} A_{a\zeta} \rho_c^\zeta} \quad (26)$$

where the full  $12 \times 12$  interaction matrix  $A_{a\zeta}$  is considered (Franciosi et al., 1980; Madec et al., 2002; Nabarro and Duesbery, 2002). The full  $12 \times 12$  interaction matrix is defined by six independent coefficients due to the symmetry of the FCC system that correspond to interactions for self-hardening dislocations (i.e.,  $A_{aa}$ ), coplanar dislocations, collinear dislocations, and dislocations that form various locks (Franciosi et al., 1980).

Furthermore, the values of the six coefficients defining  $A_{a\zeta}$  can be determined using discrete dislocation dynamics (DDD) simulations (Devincre et al., 2008; Devincre et al., 2006, 2007). While additional terms can be added to Eqs. (25) and (26) to account for

other isotropic hardening mechanisms such as the presence of (almost negligible) FCC lattice friction or dislocation bow-out stress (Mughrabi, 1987a; Mughrabi and Pschenitzka, 2005), we focus on the broadly-used isotropic hardening forms presented in Eqs. (25) and (26) to highlight the use of the proposed back stress evolution equation.

### 3.5. Dislocation density evolution

The evolution of the channel and wall dislocation densities directly influences the threshold stresses via Eqs. (25) and (26). The channel dislocation density is assumed to be comprised of primarily mobile screw dislocations while the evolved wall dislocation density is considered to be dominated by dislocations with primarily edge or mixed character (Mughrabi, 1983). Clearly, this assumption is a simplification of the complex and intricate dislocation activity occurring on the sub-micrometer scale. However, consideration of characteristic material behavior occurring over several micrometers and multiple substructure units permits the current averaged approach. We consider the dislocation densities on each slip system to evolve in accordance with several dislocation processes: multiplication, annihilation, cross slip, and rearrangement due to local load reversals.

#### 3.5.1. Dislocation multiplication

The channel (screw) and wall (edge) dislocation densities are produced via the same mechanism: dislocation bow-out from the walls spanning the substructure channel (Kuhlmann-Wilsdorf, 1962; Kuhlmann-Wilsdorf and Comins, 1983; Laird et al., 1986). This process has been proposed by multiple works (Essmann and Mughrabi, 1979; Laird et al., 1986) and is schematically described in Fig. 2 (a) for configurations at points labeled 1, 2, and 3. At point 1, a dislocation bows-out from the wall phase. Upon meeting the adjacent wall, an edge dislocation segment is deposited in the wall phase and screw dislocation segments are produced that can then glide the length of the channel phase as shown at point 3 (Laird et al., 1986). Following the dislocation multiplication functional form of Mecking and Kocks (1981), we write the multiplication rate for channel and wall dislocation densities as

$$\dot{\rho}_{c,mult}^{\alpha} = \frac{k_{c,mult}}{bl_c} \left| \dot{\gamma}_{p,c}^{\alpha} \right| \quad (27)$$

$$\dot{\rho}_{w,mult}^{\alpha} = \frac{k_{w,mult}}{bl_c} \left| \dot{\gamma}_{p,c}^{\alpha} \right| \quad (28)$$

where  $k_{c,mult}$  and  $k_{w,mult}$  are constants that control the production of dislocations, and as before,  $l_c$  refers to the mean glide distance of channel dislocations (to be defined later). As can be seen in Eqs. (27) and (28), dislocation multiplication phenomena are driven solely by the shearing rate and mean glide distance associated with the channel phase, consistent with the mechanistic process shown in Fig. 2.

#### 3.5.2. Dislocation annihilation

The channel and wall dislocation densities are assumed to decrease when dislocations of opposite sign spontaneously annihilate once within some critical distance of each other (Mecking and Kocks, 1981; Mughrabi, 1987b). However, whereas both dislocation density multiplication functions were driven by the shearing rate in the channel phase, the annihilation processes in each phase are driven by different shearing rate components, i.e.,

$$\dot{\rho}_{c,ann}^{\alpha} = \frac{2y_s}{b} \rho_c^{\alpha} \left| \dot{\gamma}_{p,c}^{\alpha} \right| \quad (29)$$

$$\dot{\rho}_{w,ann}^{\alpha} = \frac{2y_e}{b} \rho_w^{\alpha} \left| \dot{\gamma}_p^{\alpha} \right| \quad (30)$$

where  $y_s$  and  $y_e$  are the annihilation distances for screw and edge dislocations, respectively. The annihilation in the wall phase is driven by both channel and wall shearing rates to account for annihilation occurring due to limited wall plasticity as well as any recombination processes occurring as edge dislocations driven from the channel phase interact with wall dislocations. The smaller annihilation distance of edge dislocations produces a significantly larger wall dislocation density, consistent with experiments (Feaugas, 1999).

#### 3.5.3. Dislocation cross slip

Dislocation cross slip is only relevant for the channel dislocation density owing to our assumption that the channel dislocation and wall dislocation densities are primarily comprised of screw and edge dislocations, respectively. The cross slip transfer rate of channel screw dislocations considers the transfer of screw dislocations between cross slip systems  $\alpha$  and  $\zeta$ , i.e.,

$$\dot{\rho}_{c,cs}^{\alpha} = \frac{1}{2} \dot{\rho}_{c,cs}^{\alpha} \left| \dot{\gamma}_{c,\alpha}^{\zeta} \right| - \frac{1}{2} \dot{\rho}_{c,cs}^{\alpha} \left| \dot{\gamma}_{c,\alpha}^{\alpha} \right| \quad (31)$$

where the factor of  $\frac{1}{2}$  stems from our assumption that annihilation processes are considered separately in Eq. (29); Eq. (31) considers conservative dislocation cross slip. In other words, the factor of  $\frac{1}{2}$  corresponds to dislocations being transferred between cross slip systems without a reduction in dislocation density. The cross slip rate is estimated using probabilistic formulations (Kubin et al., 1992;

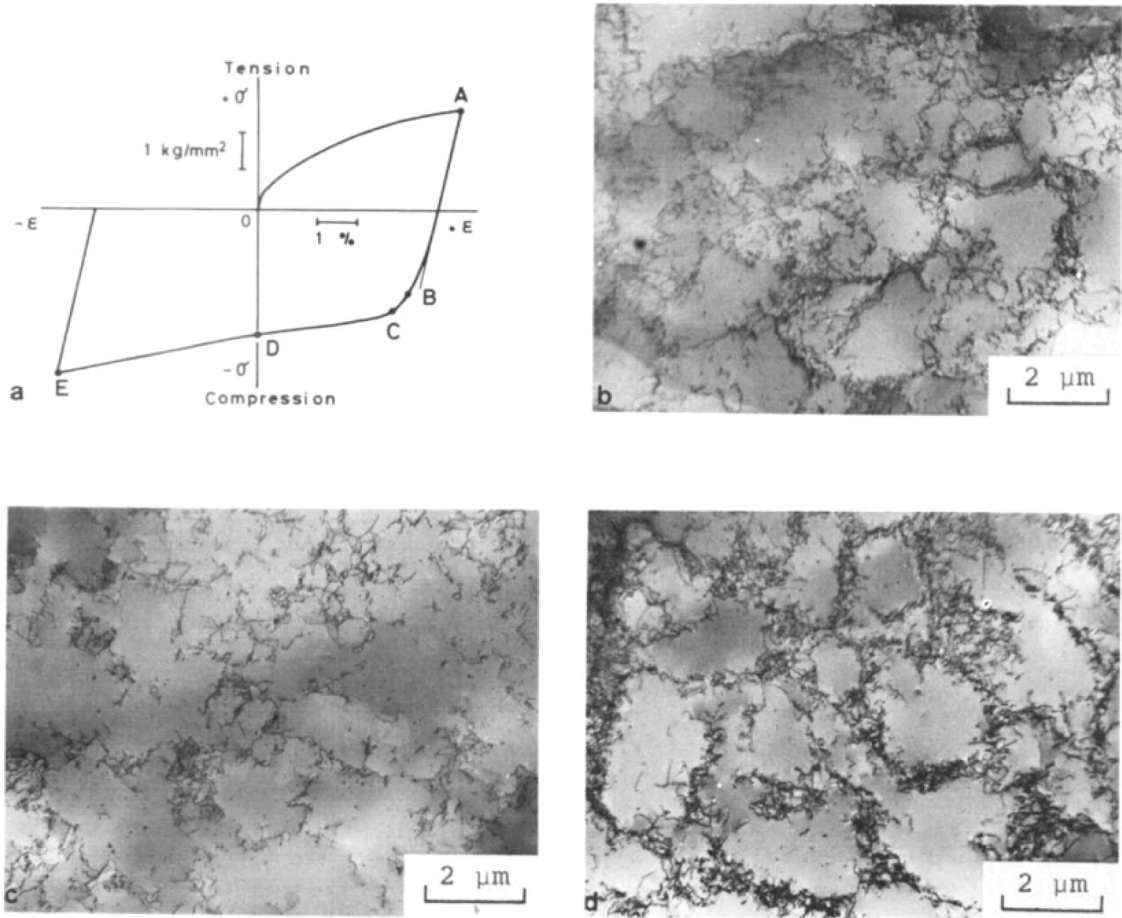


Fig. 3. TEM images taken from aluminum before and during a load reversal. Images b, c, and d correspond to points A, C, and D on the stress-strain curve. Diagram and TEM images reprinted with permission from Hasegawa et al. (1975).

Verdier et al., 1998; Zhou et al., 2010) that have been extended to consider the stress shielding from dislocation substructures (Castelluccio and McDowell, 2017) as

$$\dot{\rho}_{c,cs}^{\alpha|\zeta \rightarrow \alpha} = v_{cs} \frac{d_{struct}}{d_{cs}} \sum_{\zeta = \alpha_{cs}}^{N_{cs}} \rho_c^{\zeta} \exp \left[ -\frac{V_{cs}^{\alpha}}{k_B T} (\tau_{III} - |\tau^{\alpha} - B_c^{\alpha}|) \right] \tag{32}$$

where  $v_{cs}$  is a frequency term,  $d_{cs}$  is a reference cross slip distance,  $\alpha_{cs}$  refers to the slip system  $\zeta$  from which screw dislocations can cross slip to,  $V_{cs}^{\alpha}$  is the associated cross slip activation volume, and  $\tau_{III}$  is the critical cross slip stress. Note that  $\dot{\rho}_{c,cs}^{\alpha|\alpha \rightarrow \zeta}$  is identical in form to Eq. (32) but with the slip system indices swapped; this rate represents the cross slip activity of dislocations from slip system  $\alpha$  to slip system  $\zeta$ .

The statistical average of the cross slip activation volume is estimated as

$$V_{cs}^{\alpha} = \frac{V_{cs}^0}{|\tau^{\alpha}|} \tag{33}$$

where  $V_{cs}^0$  is the reference cross slip activation volume and has been estimated as  $20b^3 < V_{cs}^0 < 1800b^3$  for SS316L (Armstrong and Rodriguez, 2006; Bonneville et al., 1988; Rao et al., 1999; Rasmussen et al., 2000; Wang et al., 2007). The critical cross slip stress is estimated using the same process as Brown (2002), i.e.,

$$\tau_{III} = \frac{\mu b}{4\pi y_s} \tag{34}$$

### 3.5.4. Dislocation rearrangement due to load reversals

Load reversals are expected to alter both channel and wall dislocation densities as observed in experiments (Hasegawa et al., 1986).

As briefly mentioned in presenting Eq. (25), the channel hardening  $S_c^\alpha$  owes to self-interactions of pile-ups with the same sign. Upon quasi-elastic unloading with a shear stress reversal, some proportion of these pile-up dislocations collapse back towards the channel center and subsequently annihilate. This so-called “unpiling” of dislocation pile-up structures has been observed and considered in a variety of prior works (Marukawa and Sanpei, 1971; Orowan, 1959; Roberts and Barnett, 1965; Salama and Roberts, 1970). The reduction in channel dislocation density directly after a load reversal has been modeled previously (Estrin et al., 1996; Wen et al., 2016), and here we follow the micromechanically driven approach of Castelluccio and McDowell (2017). This approach utilizes the classic analytical description of dislocation pile-ups by Cottrell (1953) in concert with the substructure parameterization pursued in the current work, i.e., characterized by  $\eta$  and  $d_{struct}$ . Namely, the number of dislocations in a pile-up of length  $L$  within the channel associated with the pile-up on slip system  $\alpha$  can be estimated as (Cottrell, 1953)

$$n^\alpha = \frac{\pi L |\tau_c^\alpha|}{\mu b} \quad (35)$$

where  $\tau_c^\alpha = \tau^\alpha - B_c^\alpha$ , i.e., the channel back stress is included as a long range stress field. The dislocation pile-up length is assumed to span the substructure major axis ( $L = \eta d_{struct}$ ) and the individual dislocation length is assumed to span the substructure minor axis ( $d_{struct}$ ). As such, the dislocation density is described by the total dislocation length ( $n d_{struct}$ ) within the overall channel structure volume ( $d_{struct} \times d_{struct} \times \eta d_{struct}$ ). Combining the above relations estimates the associated pile-up dislocation density as

$$\rho_c^\alpha = \frac{\pi |\tau_c^\alpha|}{\mu b d_{struct}} \quad (36)$$

Differentiating with respect to time and considering that this mechanism operates only during quasi-elastic unloading yields the anelastic annihilation rate of channel dislocations on slip system  $\alpha$  immediately following a load reversal as

$$\dot{\rho}_{c,rev}^\alpha = Y \frac{2 |\dot{\tau}^\alpha - \dot{B}_c^\alpha|}{\mu b d_{struct}} \quad (37)$$

Here, the function  $Y = 1$  during quasi-elastic unloading and  $Y = 0$  otherwise, i.e.,  $Y = 1$  if  $\text{sgn}(\dot{\tau}^\alpha - \dot{B}_c^\alpha) \neq \text{sgn}(\tau^\alpha - B_c^\alpha)$  and 0 otherwise (Castelluccio and McDowell, 2017).

While the unpiling of dislocations in the channel phase interior occurs during initial quasi-elastic unloading of a load reversal, the rearrangement of wall dislocations occurs at a later time during the reverse loading as plastic strain begins to accumulate in the reverse direction. Careful TEM images performed on aluminum revealed a substantial decrease in the wall dislocation density following a load reversal and straining in the reverse direction (Hasegawa et al., 1975) as shown in Fig. 3. In this Figure, the TEM images b, c, and d correspond to points A, C, and D on the stress-strain curve. As seen in the TEM images, the dislocation substructure formed during the initial loading to point A rapidly untangles/dissolves upon unloading before reforming as plastic straining occurs in the reverse direction at point D. Note that some dislocation wall remnants remain in image b and the characteristic dislocation substructure dimension is similar for dislocation substructures formed in both forward and reverse directions, suggesting that memory of the substructure dimension is retained during the process (Hasegawa et al., 1975; Hasegawa et al., 1986). Similar observations regarding the rearrangement/dissolution of wall structures have been made using TEM to observe copper substructures (Chandler and Bee, 1985; Christodoulou et al., 1986). Furthermore, Gaudin and Feaugus (2004) and Gaudin et al. (2001) specifically studied the impact that dislocation substructure formation, dissolution, and reformation has on the cyclic response of materials, primarily focusing on the asymmetric load scenarios that produce ratcheting. In their work, they found that the ratcheting rate was directly related to the dissolution of wall structures and that the back stress evolution was affected by substructure formation, dissolution, and reformation processes.

This experimentally observed substructure untangling/dissolution upon load reversal motivates the proposed model framework. As discussed, the threshold stress in the walls depends on the wall dislocation density, and a decrease in the wall dislocation density following a load reversal would subsequently increase the limited plasticity occurring in the wall phase. Variations in the difference between channel and wall plastic shearing rates, i.e.,  $\dot{\gamma}_{p,c}^\alpha - \dot{\gamma}_{p,w}^\alpha$ , produce the back stress evolution per Eq. (15) that we previously categorized as necessary to adequately describe ratcheting transients.

To address partial substructure dissolution and reformation, the wall dislocation density is assumed to be comprised of immobile/irreversible ( $\rho_{w,im}^\alpha$ ) and mobile/reversible ( $\rho_{w,m}^\alpha$ ) densities with the total wall dislocation density described as

$$\rho_w^\alpha = \rho_{w,im}^\alpha + \rho_{w,m}^\alpha \quad (38)$$

The immobile/irreversible dislocation density corresponds to the heavily-tangled wall dislocations in region A of Fig. 1(b) and Fig. 2 as well as the remnant dislocation wall structure still observable in Fig. 3(c). The mobile/reversible dislocation density corresponds to the loosely-tangled wall dislocations in region C of Fig. 1(b) and Fig. 2 as well as the dislocations that disappear and subsequently reappear in Fig. 3(c)-(d).

The multiplication of each density is described, consistent with Eq. (28), as

$$\dot{\rho}_{w,mult}^\alpha = P_{im} \dot{\rho}_{w,mult}^\alpha + (1 - P_{im}) \dot{\rho}_{w,mult}^\alpha = \dot{\rho}_{w,im}^\alpha + \dot{\rho}_{w,m}^\alpha \quad (39)$$

where  $\dot{\rho}_{w,im}^\alpha = P_{im} \dot{\rho}_{w,mult}^\alpha$  and  $\dot{\rho}_{w,m}^\alpha = (1 - P_{im}) \dot{\rho}_{w,mult}^\alpha$ . Parameter  $P_{im}$  is the fraction of dislocations subsumed by the dense dislocation

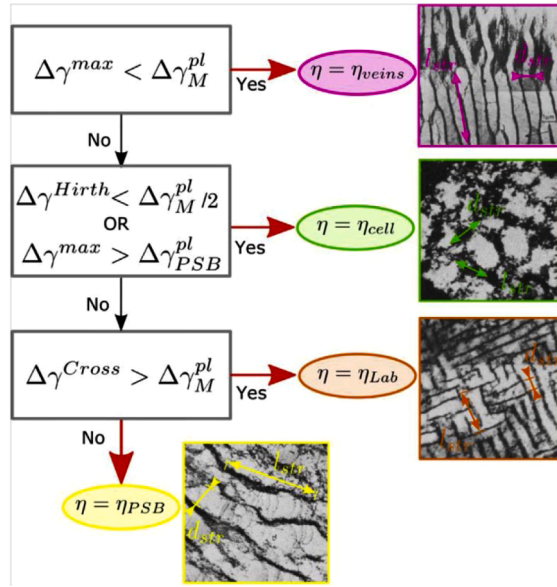


Fig. 4. Parameter  $\eta$  determination scheme used by Castelluccio and McDowell (2017) for cyclic symmetric loadings. Diagram reprinted with permission from Castelluccio and McDowell (2017).

wall core during the bow-out process that subsequently become substantially less mobile and irreversible. Estimation of  $P_{im}$  is difficult, but Kitayama et al. (2013) approximated this quantity by comparing monotonic stress-strain curves with shear reloads at various levels of pre-strain. This procedure revealed that for shear strains less than 30%, the majority of dislocations were reversible, i.e.,  $P_{im} \approx 0$ , consistent with other works (Khadyko et al., 2016; Kocks et al., 1991). Past this point,  $P_{im}$  increases nearly linearly to around 0.5 at shear strains of around 60%. To avoid undue complexity in our model, for the range of cyclic strain relative to applications of interest we assume a constant  $P_{im}$  value somewhat greater than 0. This assumption can be refined as necessary in future work.

Furthermore, following several other researchers (Barrett et al., 2020; Kitayama et al., 2013; Zecevic and Knezevic, 2015), we partition  $\rho_{w,m}^\alpha$  into two densities in order to account for load reversals and accompanying strain path changes. In accordance with our discussion of Fig. 3, we consider strain path changes to progressively untangle and reduce the mobile, reversible wall dislocation density that contributes to the isotropic wall threshold stress. To account for strain path changes, without loss of generality, we distinguish the evolution of  $\rho_{w,m}^\alpha$  dislocation density based on whether it associates with shearing in + or – directions along an assumed slip direction vector. In other words,  $\dot{\gamma}_{p,w}^\alpha$  can be either + or – depending on the arbitrarily assigned slip direction vector, and positive and negative  $\dot{\gamma}_{p,w}^\alpha$  act to generate either  $\rho_{w,m}^{\alpha+}$  or  $\rho_{w,m}^{\alpha-}$ , respectively. Consistent with our discussion regarding Fig. 3,  $\rho_{w,m}^{\alpha+}$  and  $\rho_{w,m}^{\alpha-}$  are considered to be loosely tangled in a reversible fashion, and when the strain direction reverses they untangle, reducing  $\rho_w^\alpha$  as the loose tangles re-form in the opposite direction. This treatment assumes that the mobile wall dislocations developed when  $\dot{\gamma}_{p,w}^\alpha$  has a given sign progressively untangle or recombine upon strain reversal when the sign of  $\dot{\gamma}_{p,w}^\alpha$  changes. This aspect of dissolution or partial reversibility influencing the mobile wall dislocation density is expected to be most influential during early loading cycles and is associated with back stress nonlinearity and the intense ratcheting transients observed for cycle counts on the order of tens of cycles, depending on the stress amplitude. Diminishing substructure dissolution is expected to occur as the immobile wall dislocation density  $\rho_{w,im}^\alpha$  increases.

The proposed sequence of events has been explored qualitatively before (Hasegawa et al., 1975; Hasegawa et al., 1986), and the amount of “free” rearrangement strain accompanying the partial untangling/dissolution of dislocation walls is envisioned to relate to the wall dislocation density, i.e.,  $\gamma_f^\alpha = b l_c \rho_{w,m}^\alpha$ . Rearranging the dislocation density evolution rate from this expression shows that it closely resembles the dislocation multiplication rate in Eq. (28). Consistent with this logic, we assume that directly following a load reversal, the corresponding reversible mobile wall dislocation density is reduced at a similar rate as that of the dislocation tangling processes that preceded the reversal.

### 3.5. Substructure evolution

We assume the dislocation substructure is described using three parameters:  $d_{struct}$ ,  $\eta$ , and  $f_w$ . These three parameters describe the assumed prolate spheroid size and shape as well as the volume fraction of the wall phase. Parameter  $d_{struct}$  describes the minor axis length,  $\eta$  is the ratio of the major to minor axis lengths, and  $f_w$  is the volume fraction of the wall phase. Parameter  $d_{struct}$  is used to

estimate the mean free path for channel dislocations and to calculate the evolution of both channel and wall densities. Parameter  $\eta$  is used to estimate the mean free path for channel dislocations, calculate the back stress evolution rate, and update the channel and wall dislocation densities. Parameter  $f_w$  is used to calculate the back stress evolution rate and the shearing rates in channel and wall phases. Lastly, the mean glide length of both channel and wall dislocations is discussed in this section.

There is a substantial body of work suggesting an inverse relationship between the characteristic substructure size and flow stress in both monotonic and cyclic deformation of materials that deform via wavy slip (Kayali and Plumtree, 1982; Kuhlmann-Wilsdorf, 1962). As such, the characteristic substructure length,  $d_{struct}$ , is assumed to follow a similitude scaling law (Kuhlmann-Wilsdorf, 1962; Oudriss and Feaugas, 2016; Sauzay and Kubin, 2011), i.e.,

$$d_{struct} = \frac{K_{struct}\mu b}{\max(|\tau^\alpha|) - \tau_0} \quad (40)$$

where  $K_{struct}$  is the constant of similitude that can be parameterized via TEM images and the denominator corresponds to the difference between the maximum absolute value of the resolved shear stress across all slip systems and the resolved shear stress at initial yield for the given initial material conditions and deformation temperature. Parameter  $\tau_0$  is constant and is estimated from uniaxial, monotonic single crystal simulations.

The ratio of major to minor axis lengths in the prolate spheroid structure,  $\eta$ , can be considered to define the “type” of dislocation substructure in the material. For example, for large values of  $\eta$ , the spheroids comprising the channel structure are extremely elongated and can be considered to correspond to PSB or vein-type substructure. On the other hand, smaller values of  $\eta$  correspond to labyrinth or equiaxed cell-type substructure. Prediction of the dislocation substructure is a grand challenge, especially in continuum, mesoscopic modeling frameworks (Ananthakrishna, 2007). Castelluccio and McDowell (2017) developed an accelerated scheme to assign  $\eta$  for symmetric cyclic load cases and stabilized hysteresis loops that accompany relatively high cycle counts. This scheme determined the expected dislocation structure on a cycle-by-cycle basis by evaluating and comparing the cyclic plastic shear strains on slip systems known to produce certain dislocation interactions such as Hirth locks or cross slip. This scheme is shown in the decision tree in Fig. 4. Here,  $\Delta\gamma^{max}$  is the maximum cyclic plastic shear strain amplitude among all slip systems,  $\Delta\gamma^{Hirth}$  is the cyclic plastic shear strain amplitude on slip systems that can form Hirth locks, and  $\Delta\gamma^{Cross}$  is the cyclic plastic shear strain amplitude on slip systems between which dislocations can cross slip.  $\Delta\gamma_M^{pl}$  and  $\Delta\gamma_{PSB}^{pl}$  are parameters fit with experiments that define the cyclic plastic shear strain expected to produce certain dislocation substructures.

This scheme was successfully used to predict dislocation substructures and stabilized hysteresis loops in nickel for symmetric, strain-controlled loading (Castelluccio and McDowell, 2017). However, since  $\Delta\gamma^{max}$ ,  $\Delta\gamma^{Hirth}$ , and  $\Delta\gamma^{Cross}$  are evaluated on a cycle-by-cycle basis, the evolution of  $\eta$  is not a smooth function and jumps directly between discrete values, e.g., progressing directly from  $\eta_{veins}$  to  $\eta_{cell}$ . This approach artificially accelerates dislocation substructure development and limits the use of the scheme shown in Fig. 4 to predict transient cyclic behavior that occurs from several cycles to tens of cycles. Furthermore, this approach depends on determination of the shear strain range, a quantity that may be difficult to define in general loading scenarios.

To address this, a smooth functional form is proposed to drive transient substructure development in accordance with the target steady state substructures shown in Fig. 4. A simplified expression is used to represent the role of relative slip system activation in the development of substructure, i.e.,

$$\eta = \eta_{inf} + (\eta_0 - \eta_{inf}) \exp \left[ -\chi \frac{\varepsilon_{eff,cum}^p}{k_p} \right] \quad (41)$$

where  $\eta_0$  corresponds to the initial substructure type, likely on the order of 50 for single crystals at low to moderate strain levels and is limited by grain size in the case of polycrystals due to grain boundaries reducing the mean glide distance of mobile dislocations. Furthermore,  $\eta_{inf}$  is the saturation limit for  $\eta$ , corresponding for example to equiaxed cell structure,  $\chi$  is a normalization constant,  $\varepsilon_{eff,cum}^p$  is the cumulative effective plastic strain, and  $k_p$  is a function of the relative dislocation activity on various slip systems. The parameter  $\varepsilon_{eff,cum}^p$  drives the evolution of  $\eta$  and is written as

$$\varepsilon_{eff,cum}^p = \int_{t=0}^{t=t_c} \left| \dot{\varepsilon}_{eff}^p \right| dt \quad (42)$$

where  $t$  is the simulation time and  $t_c$  is the simulation time at which  $\eta$  is being evaluated. The function  $k_p$  controls the rate at which  $\eta$  approaches  $\eta_{inf}$ . Smaller values of  $k_p$  correspond to more rapid evolution of  $\eta$  and vice versa. The parameter  $k_p$  is defined by

$$k_p = \frac{\max(\rho_c^\alpha)}{\sum_{\alpha=1}^{12} \rho_c^\alpha} \quad (43)$$

where the numerator corresponds to the maximum mobile channel dislocation density over all slip systems and the denominator corresponds to the total mobile channel dislocation density. Here, we note that Eq. (43) is a stand-in used to estimate the degree of multislip or cross slip occurring, as discussed below. Equation (41) is a phenomenological form that attempts to approximate substructure evolution by assuming the substructure development is driven by the cumulative plastic strain and evolves at a rate

determined by the severity of multi-slip or cross slip observed. (Feaugas, 1999)

In this framework, we make a simple argument that when multiple slip systems are activated or cross slip occurs, the substructure (and  $\eta$ ) evolves more rapidly towards cell-type structures, consistent with experimental observations (Feaugas, 1999; Karaman et al., 2001). Conversely, if only a single slip system is activated the substructure evolves significantly slower. This is captured by Eq. (43) in the following way: take two single crystals, one oriented along a multi-slip direction such as  $\langle 001 \rangle$  and the other oriented along a single-slip direction such as  $\langle 123 \rangle$ . Eight slip systems are equivalently activated in the crystal oriented in the  $\langle 001 \rangle$  direction, producing equivalent values of  $\rho_c^a$ . This leads to  $k_p \approx 1/8$ . On the other hand, only one slip system is activated in the crystal oriented in the  $\langle 123 \rangle$  direction. Here, the maximum  $\rho_c^a$  is experienced on the one activated slip system and is virtually equivalent to the total channel dislocation density, producing  $k_p \approx 1$ . In this case, since  $k_p$  is much smaller for the crystal oriented for multi-slip, the substructure develops in a significantly more rapid manner as expected in this case. The function  $k_p$  also takes into account the role of cross slip in substructure development. For example, if we take our  $\langle 123 \rangle$  single slip case and assume that favorable conditions for cross slip arise, the maximum  $\rho_c^a$  would decrease relative to the total channel dislocation density, decreasing  $k_p$  and accelerating substructure development. The normalization constant  $\chi$  is then used to produce reasonable substructure development rates for both crystals when compared with experiments.

The substructure evolution method proposed in Eq. (41) is only applicable for load cases producing significant cyclic plastic strain. As seen experimentally (Mughrabi, 1979; Wang et al., 1997), cyclic plastic strain ranges on the order of  $10^{-5}$  to  $10^{-2}$  generally stabilize some intermediate structure between loose, ill-defined substructures such as veins/braids and refined equiaxed cell structures. This regime is identified on cyclic stress-strain curves by a clear plateau. Clearly, Eq. (41) would not be able to resolve this plateau as any cycling that produces plastic deformation would continue to push  $\eta$  towards the equiaxed cell limit, however slowly. Nonetheless, as is observed experimentally (Lukáš et al., 1999), sufficiently high stresses and strain or asymmetric load cases almost always form cell structures, particularly in favorably oriented grains or at notches or crack tip stress risers. With our focus being on early cyclic plastic deformation situations that produce relatively significant cyclic plastic strains (e.g. transition fatigue, low cycle fatigue, and crack tip fields), we consider the simple phenomenological approach proposed in Eq. (41) as adequate. To capture stabilized hysteresis loop behavior in the plateau region of the cyclic stress-strain curve, the “lookup table” approach shown in Fig. 4 may be more appropriate.

The evolution of the wall volume fraction follows a similar approach as that adopted by other researchers (Castelluccio and McDowell, 2017; Estrin et al., 1998) and follows a similar functional form as Eq. (41), i.e.,

$$f_w = f_{\text{inf}} + (f_0 - f_{\text{inf}}) \exp \left[ \frac{-\varepsilon^{\text{eff}}}{k_f \rho_{\text{cum}}} \right] \quad (44)$$

where  $f_0$  is the initial volume fraction of walls,  $f_{\text{inf}}$  is the saturation limit, and  $k_f$  is a rate constant. Eq. (44) is a monotonically decreasing function, producing  $f_w$  behavior that may appear to be at odds with experimental results. For example, Feaugas (1999) found  $f_w$  to increase from 0 to around 40% before beginning to monotonically decrease for monotonic, uniaxial loading of SS316L at room temperature. Here, we highlight that the  $f_w$  quantity described by Eq. (44) corresponds to material regions containing primarily edge dislocations and differs from the  $f_w$  quantity extracted from TEM. In this way, assigning an  $f_0$  value of 0.5 corresponds to an initially homogenous distribution of edge and screw dislocations (Mughrabi, 1983).

The mean glide distance of channel dislocations is assumed to be limited by the mesoscale dislocation substructure (Castelluccio and McDowell, 2017), i.e.,

$$l_c = \eta d_{\text{struct}}. \quad (45)$$

On the other hand, the relatively high dislocation density in the walls severely limits the glide distance of wall dislocations. The mean glide distance is defined as (Estrin and Mecking, 1984)

$$l_w = 1 / \sqrt{\rho_w}. \quad (46)$$

The functional forms used in the mesoscopic substructure evolution framework are phenomenological in nature and are intended to capture broad trends in each of the three variables. Recent advances in lower length scale simulation capabilities, for example via continuum dislocation dynamics (CDD), potentially provide pathways for improving substructure evolution equations for CP implementation (El-Azab, 2000; Korsunsky et al., 2010; Zhou et al., 2010; Zhou et al., 2020).

### 3.6. Model overview

The model presented in the current work extends prior approaches. The equations governing the plastic deformation in the channel phase and the mesoscopic description of dislocation substructure resemble the approach used by Castelluccio and McDowell (2017). The equations governing the limited plastic deformation in the wall phase, evolution of wall dislocation density, and transient evolution of dislocation substructure are new additions. The true novelty of the framework, however, stems from the micromechanical back stress formulation that considers the plastic deformation in both channel and wall phases.

### 3.7. Parameter estimation

A concise table of all model equations is provided in Table 2 of Appendix A. Model parameters are specific to an initially well-

**Table 1**  
Parameters for an initially annealed SS316 specimen subjected to deformation at room temperature.

Direct parameters									
$\nu_G$	$b$		$C_{11}$	$C_{12}$	$C_{44}$	$C_{44@0K}$	$\mu$		
$10^{12} \text{ s}^{-1}$	2.5E-10 m		232 GPa	154 GPa	118 GPa	129 GPa	76.8 GPa		
Parameters related to atomistic mechanisms									
$F_0$	$s_0$	$p$	$q$	$y_e$	$y_s$	$d_{cs}$	$V_0^{CS}$	$P_{im}$	
1.87 eV	280 MPa	0.66	1.5	3 nm	13 nm	$10^{-5} \text{ m}$	$1000b^3$	0.15	
Interaction matrix coefficients									
Self	Coplanar		Hirth		Glissile		Lomer	Collinear	
0.122	0.122		0.07		0.137		0.122	0.625	
Parameters related to substructure evolution									
$K_{struct}$	$\eta_0$	$\eta_{inf}$	$\chi$	$f_0$	$f_{inf}$	$k_f$	$k_{c,mult}, k_{w,mult}$		
3	50	1	400	0.5	0.25	2	2		
Initial conditions									
$d_{struct,0}$				$\rho_{c,0}^a$					$\rho_{w,0}^a$
10 $\mu\text{m}$				$1 \times 10^{10} \text{ m}^{-2}$					$1 \times 10^{10} \text{ m}^{-2}$

annealed SS316L specimen deformed at room temperature and are separated into four categories as listed in Table 1:

- 1 direct parameters that are linked to underlying physics,
- 2 parameters related to atomistic mechanisms,
- 3 parameters related to mesoscale dislocation structures, and
- 4 initial conditions characterizing the well-annealed specimen structure.

The direct parameter set can be estimated from bottom-up simulations or experiments and is considered to include  $k_B$ ,  $\nu_G$ ,  $b$ , and the elastic constants. The attempt frequency  $\nu_G$  is estimated in a manner similar to that of Langer et al. (2010). The elastic constants comprising the elasticity tensor  $C$  take on values typical of x-ray diffraction measurements (Clausen et al., 1998; Daymond and Bouchard, 2006). The shear modulus  $\mu$  is computed based on the Hershey polycrystal average (Hershey, 1954; Hutchinson, 1970).

The parameters  $F_0$  and  $s_0$  are determined via calibration with the yield point in single crystal experiments (as will be seen in the results section). The profiling parameters  $p$  and  $q$  take on values typical of energy barriers considered in FCC crystal plasticity (Asaro, 1983). The annihilation distances for edge and screw dislocations are estimated from experiments (Feaugas, 1999) and atomistic simulations (Aslanides and Pontikis, 1998), respectively.  $V_0^{CS}$  is estimated in a similar manner as other researchers (Armstrong and Rodriguez, 2006). Parameter  $d_{cs}$  is assumed to be on the order of the characteristic substructure distance.  $P_{im}$  is approximated as 0.15 in accordance with the discussion of Eq. (39). The dislocation interaction coefficients comprising  $A_{\alpha\zeta}$  were determined using DDD simulations of FCC crystals at a reference dislocation density of  $1 \times 10^{12} \text{ m}^{-2}$  (Kubin et al., 2008; Madec et al., 2003). The locations of the  $A_{\alpha\zeta}$  coefficients in the interaction matrix depend on the order in which the slip systems are evaluated, but an example FCC interaction matrix can be found in the paper by Franciosi and Zaoui (1982).

The constant of similitude  $K_{struct}$  has been estimated from TEM images in a variety of contexts. Single and polycrystalline SS316L cycled at a variety of temperatures produced similitude constants ranging between 2 and 3 (Feaugas, 1999; Gorlier, 1984; Oudriss and Feaugas, 2016; Sauzay and Kubin, 2011). The origin of  $\eta_0$  and  $\eta_{inf}$  has been discussed previously and corresponds to loosely tangled veins and refined cell structure, respectively. Parameter  $\chi$  is fit using single crystal simulations as will be seen in the results section. An initial wall volume fraction ( $f_0$ ) of 0.5 is assumed. If we consider an initially annealed, homogenous material state, we assume that at the beginning of loading,  $f_w = f_c = 0.5$  and a homogenous distribution of both edge and screw dislocations exists in the material. The saturation limit and rate constant for  $f_w$  are estimated from experimental data (Ahmed et al., 2006; Feaugas, 1999; Gaudin et al., 2001; Tippelt et al., 1997). Clearly, additional DDD, CDD, or TEM data would be helpful in further refining these estimates. As a specific example, the CDD simulations executed by Xia et al. (2016) were able to predict full, three-dimensional dislocation substructures comparable to TEM images. Targeted CDD simulations of this nature have the potential to inform the dislocation substructure parameter estimates.

The current study specifically investigates SS316L specimens that have been suitably processed to be characterized by a low initial dislocation density; we assume the initial dislocation density is  $1 \times 10^{10} \text{ m}^{-2}$ . In addition, Eq. (40) is only valid once  $\max(|r^{\alpha}|) > \tau_0$ ; prior to this point, we assume  $d_{struct}$  is 10  $\mu\text{m}$  similar to prior work (Castelluccio and McDowell, 2017). Parameter  $\tau_0$ , used in Eq. (40), is approximately 80 MPa as estimated from the resolved shear stress at initial yield for single crystal simulations. Lastly, the Boltzmann constant takes on the typical value of  $1.38 \times 10^{-23} \text{ J/K}$ .

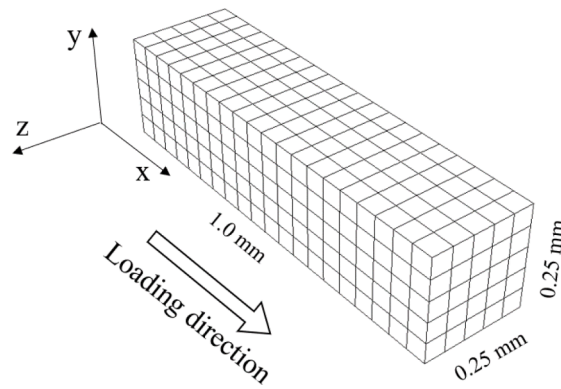


Fig. 5. Finite element mesh used for polycrystal simulations comprised of 500 C3D8R elements.

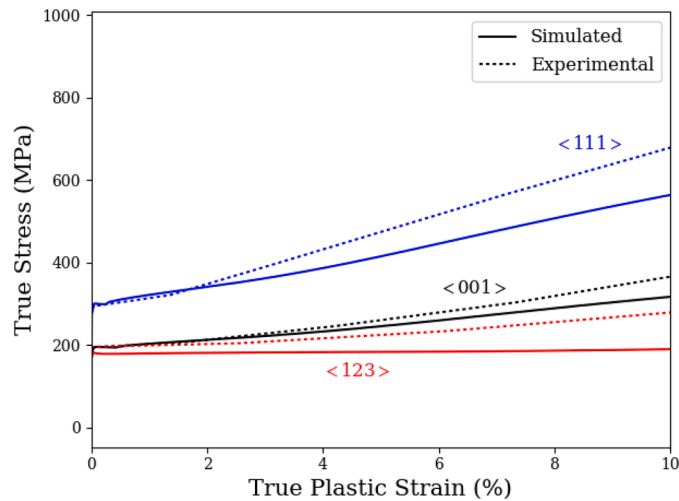


Fig. 6. Comparison between simulated and experimental data for SS316L single crystals subjected to monotonic uniaxial tension, with strain-controlled uniaxial loading in a specific crystallographic direction at room temperature. Experimental data from Karaman et al. (2001).

The philosophy of the developed framework was to root constitutive equations in physically-based mechanisms and micromechanically-motivated expressions. Accordingly, the majority of parameters are either physical constants or quantities measurable from lower-length scale simulations and experimental measurements. However, some phenomenology remains in the substructure evolution estimation. In this sense, some optimization was performed to improve the agreement between experiments and simulations. Specifically, the parameters dictating the initial yield point, i.e.,  $F_0$  and  $s_0$ , as well as the substructure evolution normalization constant  $\chi$  were optimized using a coarse guess-and-check method with experimental data.

#### 4. Case Study

The framework was tested in uniaxial load scenarios for SS316L single and polycrystals undergoing monotonic and cyclic deformation at room temperature. The constitutive equations were implemented using an ABAQUS User Material (UMAT) subroutine (Abaqus, 2011). The simulation framework was developed after similar work using UMAT models (Castelluccio et al., 2018; Castelluccio and McDowell, 2017). The single crystal simulations were performed using a single reduced integration brick element (C3D8R). The polycrystal simulations used a simple mesh of 500 reduced integration brick elements (C3D8R); the polycrystal mesh and relevant dimensions are shown in Fig. 5. For the polycrystal simulations, each element is assigned a random crystal orientation. Justification for using the relatively coarse grain representation shown in Fig. 5 is provided in Appendix B. The grain size is  $50 \mu\text{m}$ , relevant for solution treated SS316L. The influence of grain size variation is not explored in the current work, but a discussion on the influence of grain size on a similar numerical framework is available in literature (Castelluccio and McDowell, 2017). Boundary conditions were specified along the x-axis, along which periodic boundary conditions were imposed. The positive and negative y and z faces were treated as free of net traction using multi-point constraints, mimicking a uniaxial loading condition. In the following, both monotonic and cyclic loading results are presented. While the utility of the novel back stress formulation is most apparent in cyclic loading scenarios, monotonic results are presented to highlight the unifying ability of the model framework to capture a range of

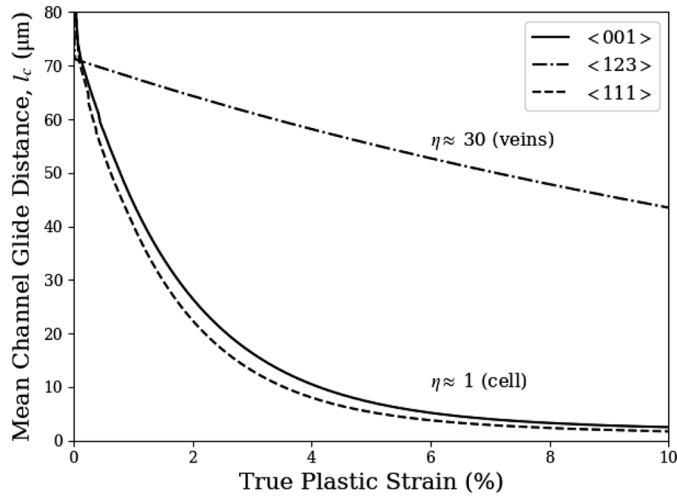


Fig. 7. Mean glide distance for mobile channel dislocations as a function of true plastic strain.

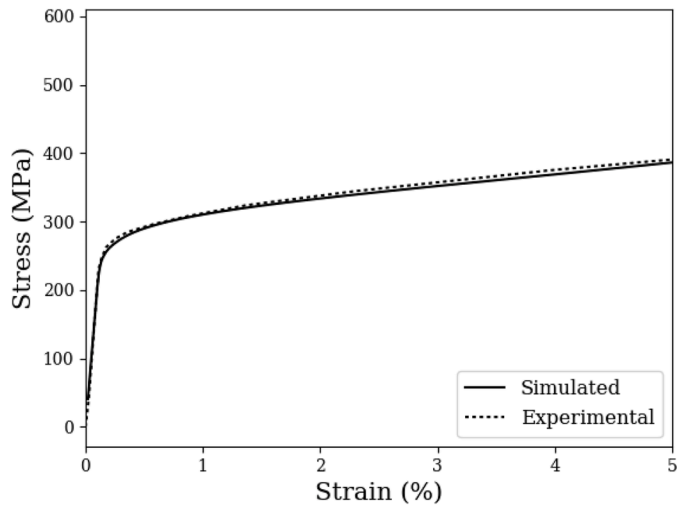


Fig. 8. Comparison between simulated and experimental data for SS316L polycrystals with random orientation distribution subjected to strain-controlled uniaxial tension deformation at room temperature. Experimental data from Kang et al. (2010).

loading conditions as well as to cross check the evolution of certain internal state variables. Lastly, while the following cyclic loading results specifically focus on the deformation response transients occurring in the first 50 cycles, selected simulations are presented for up to 100 cycles in Appendix C as an additional demonstration of framework capabilities.

#### 4.1. Monotonic single crystal deformation

Single crystal simulations were carried out with loading applied in three orientations: two orientations that promote multi-slip ( $\langle 001 \rangle$  and  $\langle 111 \rangle$ ) and one single slip ( $\langle 123 \rangle$ ). Crystals were subjected to uniaxial strain-control at a strain rate of  $5 \times 10^{-5} \text{ s}^{-1}$  at room temperature. These orientations and load parameters were chosen to facilitate comparison with the experimental data of Karaman et al. (2001); The true stress-plastic strain curves are shown in Fig. 6. Here, the simulated stress-strain curves are represented with a solid line while the experimentally measured stress-strain curves are represented with a dotted line.

As seen in Fig. 6, the initial yield point of all three orientations shows good agreement with the experimental data, suggesting the parameterization of  $F_0$  and  $s_0$  is reasonable. While the hardening rates are underestimated for all orientations, particularly the single slip  $\langle 123 \rangle$  orientation, the qualitative trends are still present. Namely, the  $\langle 111 \rangle$  orientation exhibits the highest rate of hardening while the  $\langle 123 \rangle$  orientation exhibits the lowest. Better agreement between experimental and simulated data can likely be achieved with a more comprehensive characterization of the initial material structure.

The differences in hardening rate among loading directions can be attributed to the relative activation of slip systems and corresponding dislocation substructure development in each orientation. As observed via TEM images performed by Karaman et al.

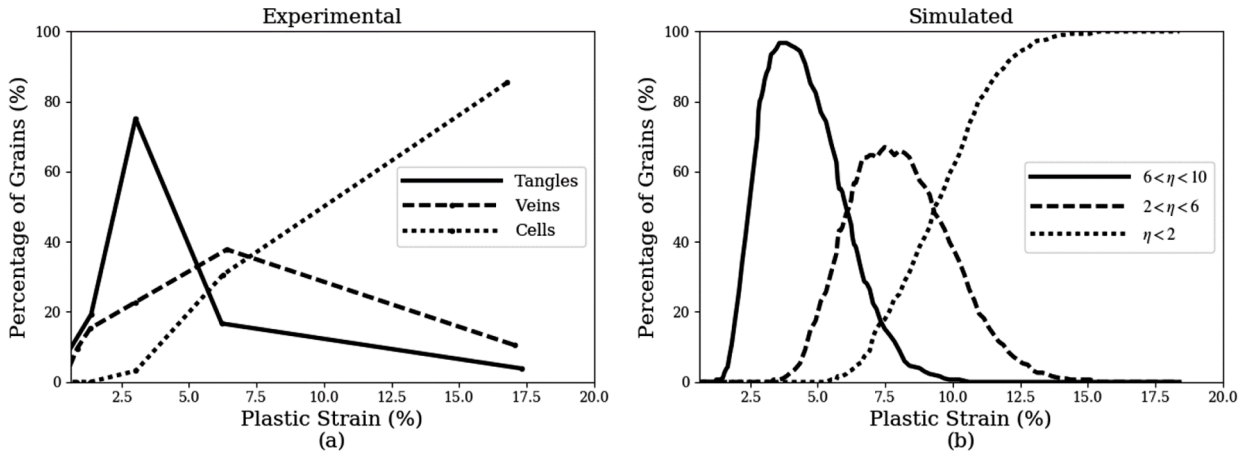


Fig. 9. Percentage of grains exhibiting certain dislocation substructure characteristics in (a) experiments and (b) simulations. Experimental data from Feaugas (1999).

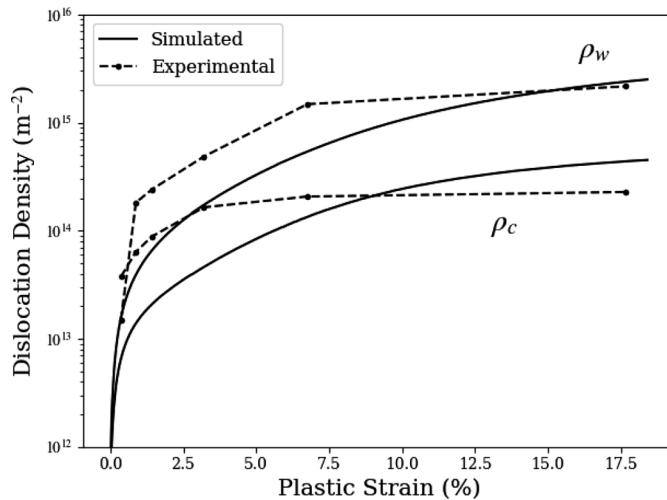


Fig. 10. Dislocation density in channels and walls as a function of plastic strain. Solid lines plot the total average dislocation density over all simulated grains. Dashed lines plot experimental data from Feaugas (1999).

(2001), the specimens loaded along the  $\langle 001 \rangle$  and  $\langle 111 \rangle$  directions were characterized by multi-slip and a tendency towards cell formation with characteristic substructure distances on the order of 0.1 to 1  $\mu\text{m}$  at a true plastic strain of around 10%. On the other hand, only one system was primarily activated in the specimen loaded in the  $\langle 123 \rangle$  direction, producing a material state largely absent of a well-organized dislocation substructure. Consistent with the mesh length theory of strain hardening (Kuhmann-Wilsdorf and Comins, 1983), the mean dislocation glide distance is substantially limited by the dislocation substructure for the specimens loaded along the  $\langle 001 \rangle$  and  $\langle 111 \rangle$  directions, producing the higher rate of work hardening. To demonstrate how the proposed framework captures this phenomenon, the mean glide distance for channel dislocations,  $l_c$ , is plotted as a function of true plastic strain as shown in Fig. 7. Here, the multi-slip conditions experienced in the specimens loaded along the  $\langle 001 \rangle$  and  $\langle 111 \rangle$  directions produce rapid substructure development in accordance with Eq. (41). For these loading orientations, the  $\eta$  value approximates channel dislocation substructures at a true plastic strain of roughly 10%. Alternatively, the single slip conditions experienced in the specimen loaded along the  $\langle 123 \rangle$  direction precludes significant dislocation substructure development with the  $\eta$  value approximating something akin to loose veins or braids at a true plastic strain of roughly 10%.

#### 4.2. Polycrystal monotonic deformation

A simulated polycrystal was subjected to room temperature, strain-controlled loading using the same loading parameters as Kang et al. (2010), i.e., a prescribed strain rate of  $2 \times 10^{-3} \text{ s}^{-1}$ . The engineering stress-strain curves for both simulated and experimental data are shown in Fig. 8. Here, the simulated stress-strain curve is represented with a solid line while the experimental stress-strain

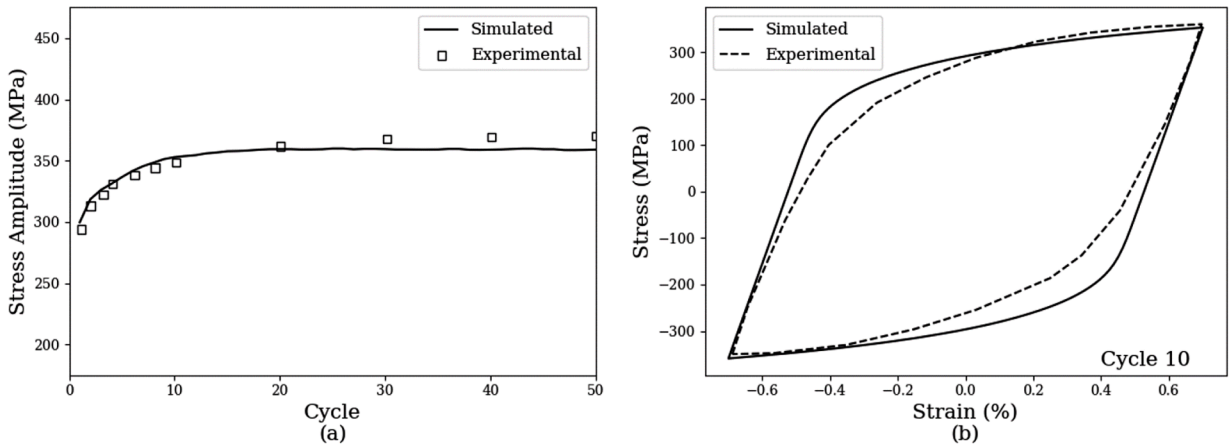


Fig. 11. Comparison between simulated and experimental results for fully reversed strain-controlled cyclic loading of SS316L polycrystals in the absence of a mean stress. Experimental data from Kang et al. (2011).

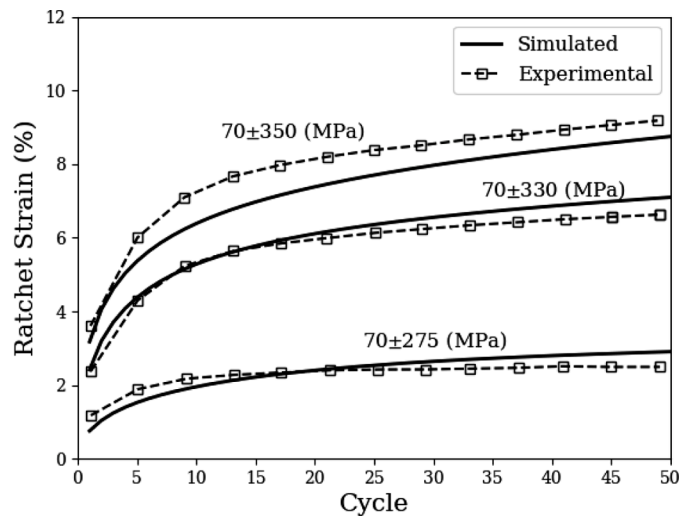


Fig. 12. Comparison between simulated and experimental results for stress-controlled asymmetric cyclic loading of SS316L polycrystals with constant mean stress. Experimental data from Kang et al. (2011).

curve is represented with a dotted line.

As can be seen in Fig. 8, the averaged, macroscale response of the single crystal behavior exhibited in Fig. 6 matches closely with experimental data when a sufficient number of crystals are sampled. The proposed framework can be further examined through comparison with the in-depth investigation of uniaxial, monotonic SS316L deformation conducted by Feaugas (1999). To facilitate comparison, the strain-controlled loading was changed to match the loading condition used in this study, namely a prescribed strain rate of  $4 \times 10^{-4} \text{ s}^{-1}$ .

First, the percentage of grains exhibiting particular dislocation substructures can be qualitatively compared as shown in Fig. 9. In Fig. 9(a), the percentage of grains exhibiting certain dislocation structures as determined via TEM is plotted as a function of plastic strain. Note that Feaugas (1999) distinguished between three different types of characteristic substructures, i.e., tangles, walls, and cells. Here, we note that while the term “walls” generally refers to the dislocation-dense phase, Feaugas (1999) used this term to refer to something akin to a vein substructure. Pham et al. (2013) similarly used the terms “walls” and “veins” interchangeably. In Fig. 9b, we assume that  $\eta$  is a surrogate for these substructures and discretely bin  $\eta$  in order to make a comparison with experimental data. While we note that the limits used to bin the continuous  $\eta$  evolution are relatively arbitrary for the wall/vein and tangle substructures, the purpose of this comparison is to show the  $\eta$  evolution rate described by Eq. (41) is reasonable when qualitatively compared with the evolution of substructures measured in experiments.

The dislocation densities in channel and wall phases are also compared with experiments, as shown in Fig. 10. This plot shows the relevant dislocation densities plotted as a function of plastic strain. The simulated dislocation densities correspond to the total dislocation density over all slip systems and averaged over all grains. As can be seen, simulations exhibit order of magnitude agreement

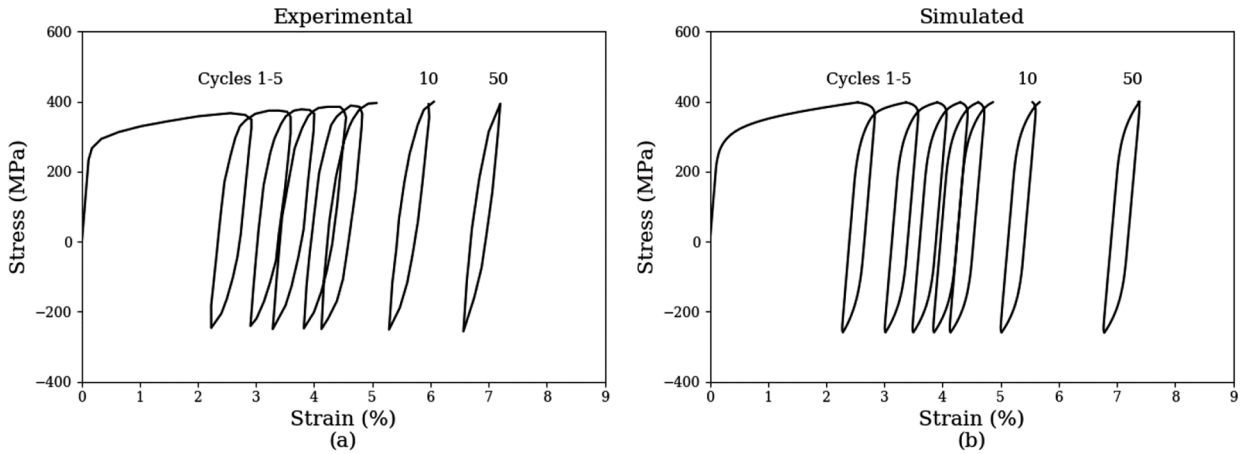


Fig. 13. Comparison between experimental (a) and simulated (b) hysteresis loop evolution for cycles 1-5, 10, and 50 for the 70±330 MPa load history.

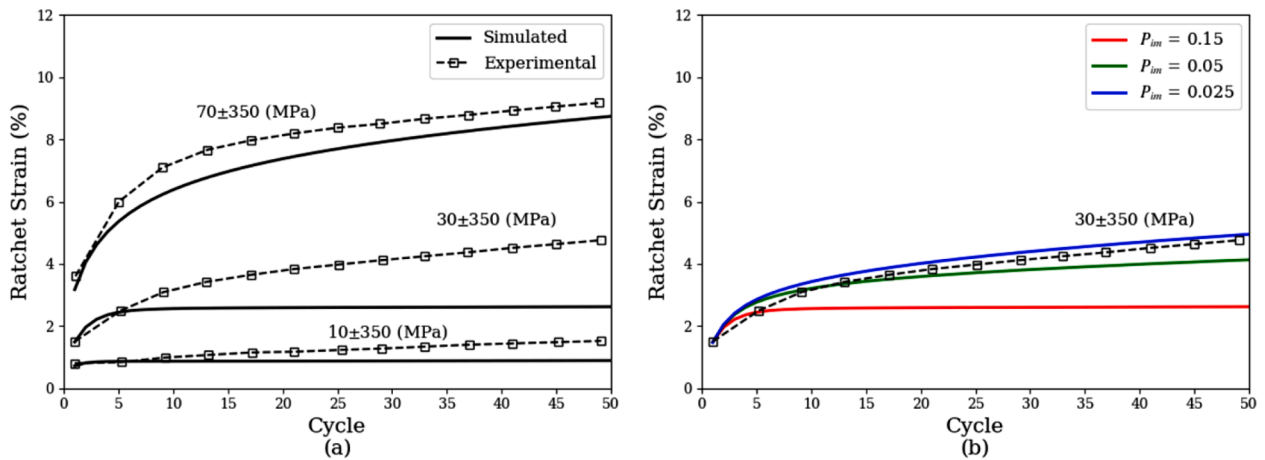


Fig. 14. (a) Comparison between simulated and experimental results for stress-controlled asymmetric cyclic loading and a constant stress amplitude for SS316L polycrystals. (b) Influence of  $P_m$  on the rate of ratchet strain accumulation for stress-controlled cyclic loading with low mean stress. Experimental data from Kang et al. (2011).

with experimental results.

Clearly, the proposed model contains substantial information regarding dislocation substructure and its evolution with respect to underlying crystallography during imposed deformation.

### 4.3. Polycrystal fully reversed strain-controlled cyclic loading

A simulated polycrystal was subjected to room temperature, fully reversed strain-controlled cyclic loading using the same loading parameters as Kang et al. (2011), i.e., a strain rate of  $2 \times 10^{-3} \text{ s}^{-1}$  and a strain amplitude of 0.7%. The stress amplitude vs. cycle number data and a characteristic hysteresis loop extracted at cycle 10 are shown in Fig. 11. It should be noted that the yield point is less distinguishable in the experimental hysteresis loop when compared to the simulated one in Fig. 11(b). This insufficiency in the model framework has been recognized in prior work (Dong et al., 2014; Ren et al., 2020) as owing to the inclusion of only a single back stress component. Multiple components of back stress considering short- and long-range transients can be introduced to resolve the initial elastic-plastic transition, but this is not a focus in the current work.

### 4.4. Polycrystal stress-controlled loading with a mean stress

A simulated polycrystal was subjected to room temperature, stress-controlled cyclic loading with a positive load ratio and associated mean stress, using the same loading parameters as Kang et al. (2010), i.e., a prescribed stress rate of  $400 \text{ MPa s}^{-1}$  and a variety of stress amplitudes for a mean stress of 70 MPa. The ratchet strain vs. cycle number curve data are plotted in Fig. 12. Note that the ratchet

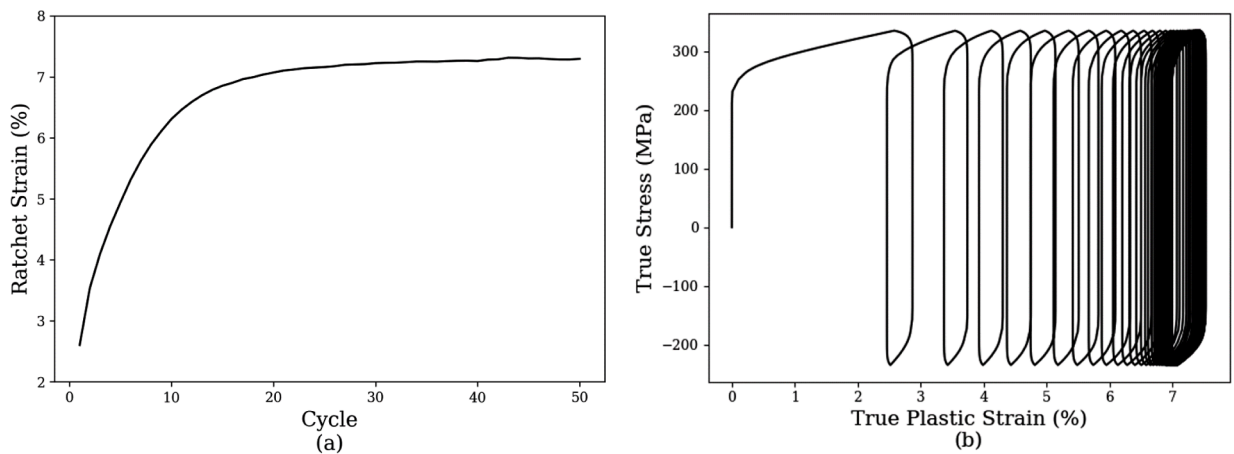


**Fig. 15.** (a) Ratchet strain plotted as a function of cycle number and (b) True-stress plastic strain curve for a SS316L single crystal loaded along the  $\langle 001 \rangle$  for stress-controlled loading at  $50 \pm 285$  MPa and a stress rate of  $400 \text{ MPa s}^{-1}$  at room temperature.

strain is defined as  $\epsilon_r = (\epsilon_{\max} + \epsilon_{\min})/2$  where  $\epsilon_{\max}$  and  $\epsilon_{\min}$  are the maximum and minimum engineering strains in each cycle, respectively.

In addition to the ratchet strain vs. cycle number data, the hysteresis loop evolution for the  $70 \pm 330$  MPa load history is shown in Fig. 13. Note that both experimental and simulated hysteresis loops are rounded near the maximum tensile stress due to viscoplastic effects. As seen in these two figures, the proposed model appears to predict the ratchet behavior relatively well for the simulated load histories.

A second set of simulations were conducted assuming a constant stress amplitude of 350 MPa with several values of mean stress and a loading rate of  $400 \text{ MPa s}^{-1}$ . The results from these simulations are shown along with experimental data from Kang et al. (2010) in Fig. 14. As seen in Fig. 14(a), the prediction of ratchet strain accumulation is less accurate at lower mean stresses. Indeed, while the simulations predict a nearly constant ratchet strain achieved from cycle 5 onward for the  $30 \pm 350$  MPa case, the experimental data suggest a relatively high level of steady state ratchet strain accumulation.

Lower accuracy of simulated ratchet strain accumulation for low mean stresses is likely due to the simple approximation adopted for the  $P_{im}$  parameter. As discussed in presenting Eq. (39), we assumed that  $P_{im}$  was constant and somewhat greater than 0 based on the work of Kitayama et al. (2013). However,  $P_{im}$  effectively modulates the degree of substructure dissolution and reorganization upon a load reversal; assuming a constant value regardless of pre-strain and loading parameters is likely an oversimplification. Kitayama et al. (2013) suggested that  $P_{im}$  steadily increases as a function of strain preceding a load reversal due to the accumulation of dislocation debris and for low pre-strains is nearly 0. Gaudin and Feaugas (2004) suggested that the severity of substructure dissolution at low mean stresses is a more complex phenomenon that results from the competition between the degree of reverse plastic strain and required stress to break wall dislocation patterns. Specifically, while low mean stresses produce high amounts of reverse plastic strain, aiding in the dissolution process, the low mean stress produces local stresses that are more likely to remain below the threshold required to break wall dislocation configurations.

While we do not pursue a more rigorous formulation for  $P_{im}$  in the current work, we demonstrate in Fig. 14(b) that the proposed model's prediction of low mean stress ratcheting behavior is improved upon proper choice of the  $P_{im}$  parameter. In this plot, three ratchet strain vs. cycle number curves are plotted for three different  $P_{im}$  values for the  $30 \pm 350$  MPa case. The red, green, and blue curves correspond to  $P_{im}$  values of 0.15, 0.05, and 0.025, respectively. Note that a  $P_{im}$  value of 0.15 corresponds to the  $P_{im}$  value used in the other simulations presented herein. As can be seen in Fig. 14(b), decreasing  $P_{im}$  (increasing degree of dissolution) increases the quality of the model prediction and can be interpreted as being representative of the pre-strain arguments of Kitayama et al. (2013) or mean stress arguments of Gaudin and Feaugas (2004). Accordingly, this work has established that the ratcheting rate is clearly linked to dissolution parameter  $P_{im}$ .

Further parameterization of  $P_{im}$  is likely difficult to achieve from a top-down approach using additional macroscopic experiments. On the other hand, lower-length scale simulation techniques such as atomistics or DDD are likely limited in their usefulness due to both length and time scale restrictions. However, CDD simulations such as the ones performed by Xia et al. (2016) have demonstrated an ability to predict three-dimensional dislocation substructures and extract metrics that can be useful in mesoscale crystal plasticity frameworks. A more rigorous formulation for  $P_{im}$  can likely be developed using CDD simulations of this nature.

#### 4.5. Single crystal asymmetric stress-controlled loading

The foregoing has demonstrated that the proposed model can adequately predict a range of material behavior pertaining to monotonic and cyclic loading of single and polycrystals. In this section, we elucidate how the back stress model is able to predict ratcheting behavior without relying on common phenomenological kinematic hardening forms and associated fitting parameters. To this end, we load a SS316L single crystal along the multi-slip orientation investigated earlier, i.e.,  $\langle 001 \rangle$ , for stress-controlled loading

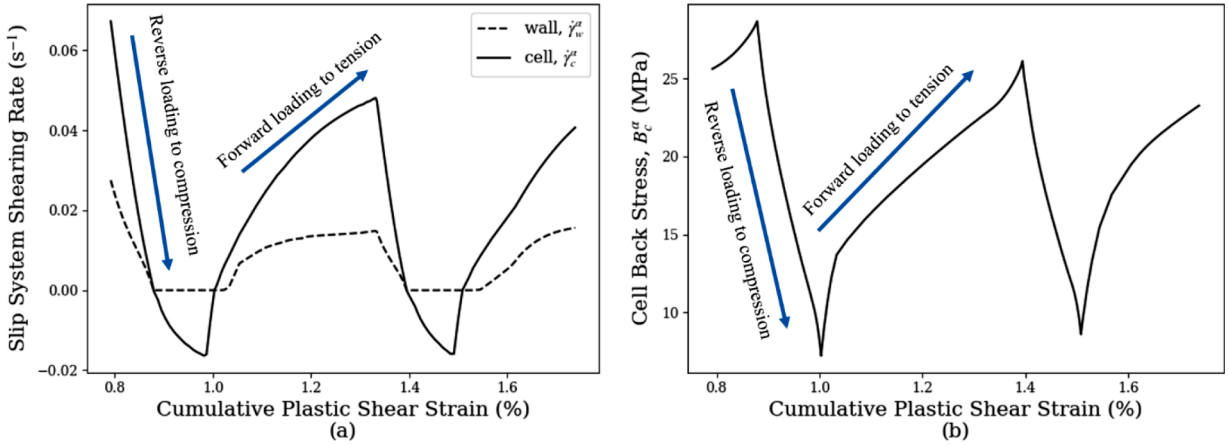


Fig. 16. Slip system shearing rates and back stress in the channel phase as a function of cumulative plastic shear strain.

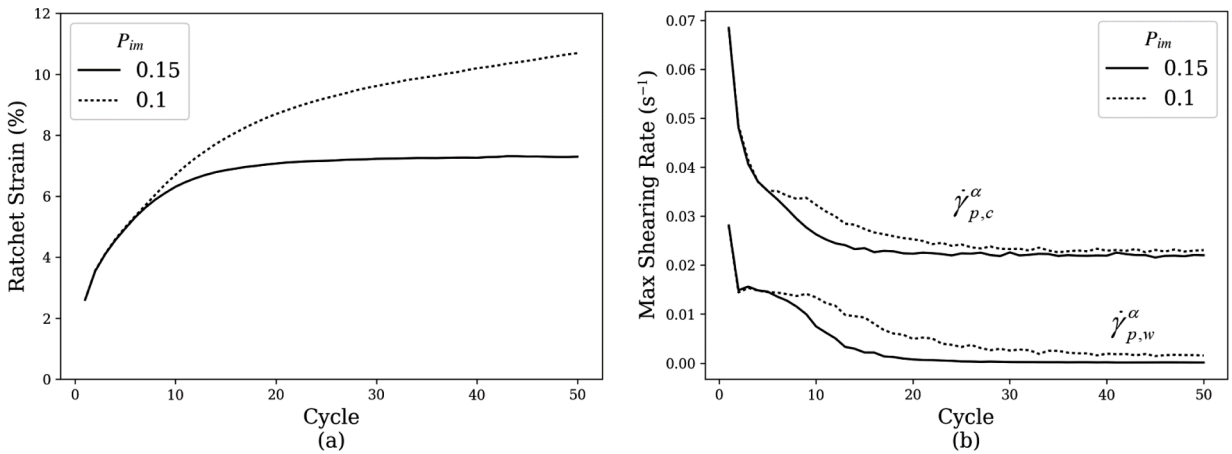


Fig. 17. Ratchet strain (a) and maximum slip shearing rate over each cycle for both channel and wall phases (b) plotted as a function of cycle number for two different  $P_{im}$  values. Data were extracted along one of the equivalently activated slip systems in the current single crystal load configuration.

defined by  $50 \pm 285$  MPa at a stress rate of  $400 \text{ MPa s}^{-1}$ . The ratchet strain vs. cycle number and true stress vs. true plastic strain curves are shown in Fig. 15.

The wall and channel slip system shearing rates as well as the channel back stress evolution are plotted as a function of cumulative plastic shear strain specifically for cycles 2 and 3 in Fig. 16(a) and (b) respectively. In these plots, the data were extracted from one of the activated slip systems in the chosen multi-slip orientation. The choice of slip system for data extraction is arbitrary due to the activation of multiple equivalent slip systems in this highly symmetric loading orientation. In addition to the plotted curves, blue arrows are provided to differentiate between load segments, i.e., distinguishing between reverse loading to compression and forward loading to tension.

The evolution of the values shown in Fig. 16 reveal the fundamental model behavior that produces ratcheting. Simply put, the lack of plastic deformation in the wall phase during reverse loading to compression produces a relatively fast and linear evolution of the channel back stress per Eq. (15). On the other hand, the moderate amount of plastic deformation in the wall phase during forward loading to tension produces relatively slow and nonlinear evolution of the channel back stress. Ignoring more complex variable evolution, this can be written symbolically as  $B_c^\alpha = f_{wf}(\eta, f_{accom}^\alpha)(\dot{\gamma}_{p,c}^\alpha - \dot{\gamma}_{p,w}^\alpha)$  and for the load scenario considered here,  $(\dot{\gamma}_{p,c}^\alpha - \dot{\gamma}_{p,w}^\alpha)_{forward} < (\dot{\gamma}_{p,c}^\alpha - \dot{\gamma}_{p,w}^\alpha)_{reverse}$ . In essence, the difference in the channel back stress evolution in forward and reverse directions due to the wall phase plastic behavior produces ratcheting in the proposed model.

The ratchet strain transient observed in Fig. 12, Fig. 14, and Fig. 15(a) is associated with progressive stabilization of the dislocation substructure and subsequent decrease in the degree of substructure dissolution with each load reversal. As the wall dislocation density becomes increasingly tangled and immobilized, plastic deformation becomes more difficult to initiate and the wall plasticity to which

we attributed the ratcheting behavior diminishes. This process was briefly discussed in relation to Fig. 14 and is now highlighted in Fig. 17. Here, the ratchet strain and maximum slip system shearing rates over each cycle are plotted as a function of cycle number for two different  $P_{im}$  values. In this case, we consider  $P_{im}$  to represent the severity of substructure dissolution with larger values corresponding to faster stabilization of the substructure via faster evolution of the immobile/irreversible wall dislocation density  $\rho_{w,im}^a$ .

As can be seen in Fig. 17(a), the nonlinearity in both curves is exhausted by cycle 20 and can be directly correlated to the variation in slip system shearing rates shown in Fig. 17(b). For the case of  $P_{im}=0.15$  (solid curve),  $\dot{\gamma}_{p,w}^a$  approaches a very low shearing rate until it is negligible at around cycle 20. This corresponds directly to the effective cessation of meaningful ratchet strain accumulation. On the other hand, for the case of  $P_{im}=0.1$  (dotted curve),  $\dot{\gamma}_{p,w}^a$  is larger than for the  $P_{im}=0.15$  case and results in the steady accumulation of cyclic creep strain observed. In terms of dislocation substructure stabilization, the degree of substructure dissolution diminishes to a negligible amount for the  $P_{im}=0.15$  case while it reaches some non-zero steady state value for the  $P_{im}=0.1$  case. The observations regarding dislocation substructure stabilization were based on the different shearing rate behavior noted at higher cycle counts in Fig. 17.

Taken together, Fig. 16 and Fig. 17 shed light on how the model is able to capture ratcheting. Essentially, the model predicts nonlinear back stress evolution and associated ratcheting based on the degree of plasticity occurring in the wall phase, intimately related to the threshold stress in both phases,  $S_c^c$  and  $S_w^c$ . The extent of transient ratcheting behavior is due to accumulation of irreversible, heavily tangled wall edge dislocations. Steady state cyclic creep conditions can be achieved due to a stabilization of the dislocation substructure dissolution and formation processes accompanied with low-level, continued plastic wall deformation.

## 5. Conclusions

This work builds on previous micromechanically-based back stress formulations (Castelluccio and McDowell, 2017; Sauzay, 2008), further attributing complex cyclic plasticity responses such as ratcheting under stress-controlled cycling in the presence of mean stress to the relative ability of both channel and wall phases to plastically deform. The proposed micromechanical back stress evolution does not rely on phenomenological forms such as the AF model, and naturally evolves as a function of the plastic flow behavior in channel and wall phases.

In addition, the proposed model framework removes phenomenological fitting constants in the back stress formulation where they have unclear micromechanical origins and instead limits the majority of phenomenology to the approximation of substructure shape and size which can be directly informed via TEM imaging or simulated using CDD. In this way, the proposed model has enhanced utility as a scientific tool to investigate dislocation substructures and activity occurring on the mesoscale.

We applied the proposed back stress model to explore possible mechanisms responsible for the ratcheting behavior in SS316L. We attribute the ratcheting behavior of SS316L (and by proxy a multitude of FCC materials that deform by means of wavy slip) to the cyclic formation, dissolution/rearrangement, and reformation of dislocation substructures. This attribution is consistent with:

- i) the in-depth experimental studies by Gaudin and Feaugas (2004), Feaugas (1999), and Hasegawa et al. (1975) amongst others,
- ii) the qualitative treatment of dislocation substructure pioneered by Mughrabi (1983) and Hasegawa et al. (1986), and
- iii) strain-path dependent dislocation evolution considered by a variety of authors (Barrett et al., 2020; Kitayama et al., 2013; Zecevic and Knezevic, 2015).

By accounting for the evolution of dislocation substructure morphology and its resistance to dislocation plasticity, the proposed framework introduces wall plasticity and corresponding back stress behavior associated with wall dissolution and reformation that reproduced experimental ratcheting data well. In addition, the model was shown to have good agreement with monotonic single crystal experiments as well as monotonic and cyclic polycrystal experiments that considered both fully reversed strain-controlled cycling and stress-controlled cycling with mean stress.

Finally, we note that the incorporation of the substructure dissolution based on the sign of the slip system shearing rate is bound to have ramifications for modeling deformation-induced anisotropy of crystalline response for changes of loading path, which has long been a substantial challenge to modeling with crystal plasticity and reduced order anisotropic yield surfaces. Application of the present formulation to complex nonproportional strain histories is likely to produce non-intuitive and physically meaningful results, serving as a potential area for subsequent framework extension and application.

## CRedit authorship contribution statement

**Theodore Zirkle:** Conceptualization, Methodology, Software, Visualization, Writing – original draft. **Ting Zhu:** Conceptualization, Investigation, Writing – review & editing. **David L. McDowell:** Supervision, Writing – review & editing.

## Declaration of Competing Interest

The authors declare that they have no known competing financial interests or personal relationships that could have appeared to influence the work reported in this paper.

**Acknowledgements**

We acknowledge the financial support of Naval Nuclear Laboratory, operated by Fluor Marine Propulsion, LLC for the US Naval Reactors Program, particularly discussions with Dr. Benjamin Anglin. We also acknowledge the foundational work of Dr. Castelluccio in the formulation of microstructure-sensitive crystal plasticity models.

**Appendix A**

**Table 2**  
Summary of model equations.

Flow rule Parameter	Equation
Plastic shearing rate	$\dot{\gamma}_{p,c}^\alpha = \dot{\gamma}_{c,0}^\alpha \exp \left[ -\frac{F_0}{k_B T} \left( 1 - \left[ \frac{\tau_{c,eff}^\alpha}{s_0 \frac{\mu_{00K}^\alpha}{\mu}} \right]^p \right)^q \right] \text{sgn}(\tau^\alpha - B_c^\alpha)$ $\dot{\gamma}_{p,w}^\alpha = \dot{\gamma}_{w,0}^\alpha \exp \left[ -\frac{F_0}{k_B T} \left( 1 - \left[ \frac{\tau_{w,eff}^\alpha}{s_0 \frac{\mu_{00K}^\alpha}{\mu}} \right]^p \right)^q \right] \text{sgn} \left( \tau^\alpha + \frac{1-f_w}{f_w} B_c^\alpha \right)$
Reference shearing rate	$\dot{\gamma}_{c,0}^\alpha = \rho_c^\alpha l_c b v_G$ $\dot{\gamma}_{w,0}^\alpha = \rho_{w,m}^\alpha l_w b v_G$
Effective resolved shear stress	$\tau_{c,eff}^\alpha = ( \tau^\alpha - B_c^\alpha  - S_c^\alpha)$ $\tau_{w,eff}^\alpha = ( \tau^\alpha + \frac{1-f_w}{f_w} B_c^\alpha  - S_w^\alpha)$
Threshold stress	$S_c^\alpha = \mu b \sqrt{A_{aa} \rho_c^\alpha}$ $S_w^\alpha = \mu b \sqrt{\sum_{c=1}^{12} A_{ac} \rho_c^\alpha}$
Back stress	$\dot{B}_c^\alpha = f_w f(\eta, f_{accum}) (\dot{\gamma}_{p,c}^\alpha - \dot{\gamma}_{p,w}^\alpha)$ $\dot{B}_w^\alpha = -\frac{1-f_w}{f_w} \dot{B}_c^\alpha$
Dislocation density evolution Parameter	Equation
Dislocation density evolution	$\dot{\rho}_c^\alpha = \dot{\rho}_{c,mult}^\alpha - \dot{\rho}_{c,ann}^\alpha + \dot{\rho}_{c,cs}^\alpha - \dot{\rho}_{c,rev}^\alpha$ $\dot{\rho}_w^\alpha = \dot{\rho}_{w,mult}^\alpha - \dot{\rho}_{w,ann}^\alpha - \dot{\rho}_{w,rev}^\alpha$
Dislocation multiplication	$\dot{\rho}_{c,mult}^\alpha = \frac{k_{c,mult}}{b l_c} \left  \dot{\gamma}_{p,c}^\alpha \right $ $\dot{\rho}_{w,mult}^\alpha = \frac{k_{w,mult}}{b l_c} \left  \dot{\gamma}_{p,c}^\alpha \right , \dot{\rho}_{w,mult}^\alpha = P_{im} \dot{\rho}_{w,mult}^\alpha + (1 - P_{im}) \dot{\rho}_{w,mult}^\alpha = \dot{\rho}_{w,im}^\alpha + \dot{\rho}_{w,m}^\alpha$
Dislocation annihilation	$\dot{\rho}_{c,ann}^\alpha = \frac{2\gamma_s}{b} \rho_c^\alpha \left  \dot{\gamma}_{p,c}^\alpha \right $ $\dot{\rho}_{w,ann}^\alpha = \frac{2\gamma_e}{b} \rho_w^\alpha \left  \dot{\gamma}_p^\alpha \right $
Dislocation cross slip	$\dot{\rho}_{c,cs}^\alpha = \frac{1}{2} \dot{\rho}_{c,cs}^{\alpha \zeta \rightarrow \alpha} - \frac{1}{2} \dot{\rho}_{c,cs}^{\alpha \alpha \rightarrow \zeta}$ $\dot{\rho}_{c,cs}^{\alpha \zeta \rightarrow \alpha} = v_{cs} \frac{d_{struct}}{d_{cs}} \sum_{\zeta=\alpha_0}^{N_{cs}} \rho_c^\zeta \exp \left[ -\frac{V_{cs}^\alpha}{k_B T} (\tau_{III} -  \tau^\alpha - B_c^\alpha ) \right]$
Load reversal dislocation evolution	$\dot{\rho}_{c,rev}^\alpha = \gamma \frac{2 \dot{\gamma}^\alpha - \dot{B}_c^\alpha }{\mu b d_{struct}}$ $\dot{\rho}_{w,rev}^\alpha = \frac{k_{w,mult}}{b d_{struct}} \left  \dot{\gamma}_{p,c}^\alpha \right $
Substructure evolution Parameter	Equation
Characteristic substructure dimension	$d_{struct} = \frac{K_{struct} \mu b}{\max( \tau^\alpha ) - \tau_0}$
Substructure aspect ratio	$\eta = \eta_{inf} + (\eta_0 - \eta_{inf}) \exp \left[ -\chi \frac{\epsilon_{p,cum}^{eff}}{k_\rho} \right],$ $k_\rho = \frac{\max(\rho_c^\alpha)}{\sum_{\alpha=1}^{12} \rho_c^\alpha}$
Wall volume fraction	$f_w = f_{inf} + (f_0 - f_{inf}) \exp \left[ \frac{-\epsilon_{p,cum}^{eff}}{k_f} \right]$
Mean glide distance	$l_c = \eta d_{struct}$ $l_w = 1/\sqrt{\rho_w}$

**Appendix B**

The finite element mesh shown in Fig. 5 assumes one element per grain, corresponding to a relatively coarse grain representation in view of the reduced integration method employed here. Simplifying the microstructure in this manner was done to reduce the significant computation time required to explicitly model tens of load cycles, and Sauzay et al. (2014) showed that similar simplified microstructure representations adequately represent macroscopic response as well as the cumulative probability distribution of mean plastic strain per grain. More recent works have similarly found equivalent distributions of fatigue indicator parameters at the grain level for varying degrees of microstructure fidelity (Castelluccio and McDowell, 2015) as well as similar macroscopic stress-strain curves for simulated specimens undergoing cyclic loads (Castelluccio and McDowell, 2017).

Regardless, a limited set of simulations were performed for various levels of mesh refinement for completeness. The various grain representations simulated are shown in Fig. 18 where each color corresponds to a different grain orientation. The microstructure representations shown in Fig. 18 were produced using DREAM.3D (Groeber and Jackson, 2014) where an equiaxed grain structure with a mean grain diameter of 62 μm was assumed. The influence of varying the microstructure fidelity was studied by comparing responses for two load scenarios. Strain-controlled monotonic loading at a prescribed strain rate of  $2 \times 10^{-3} \text{ s}^{-1}$  to 5% strain is shown in Fig. 19(a), and stress-controlled cyclic loading at a prescribed stress rate of  $400 \text{ MPa s}^{-1}$  for a mean stress of 70 MPa and stress amplitude of 330 MPa is shown in Fig. 19(b). Note that the most refined mesh was only run for 7 cycles in Fig. 19(b) due to the significant computational demand of explicitly simulating load cycles using this mesh. The results shown in Fig. 19 demonstrate only relatively limited changes of predicted work hardening and ratchet response with substantial mesh refinement within grains, consistent with prior assertions (Castelluccio and McDowell, 2015; Castelluccio and McDowell, 2017; Sauzay et al., 2014).

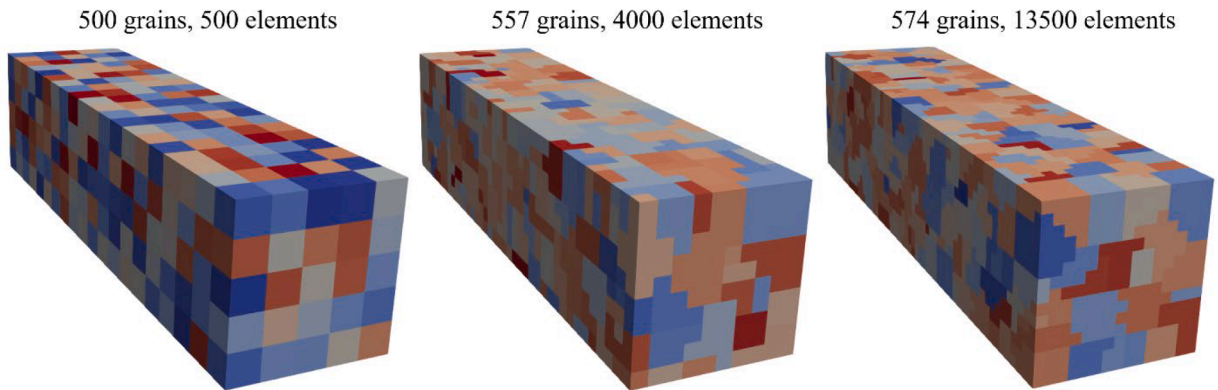


Fig. 18. Grain representations used to study the influence of microstructure fidelity on the simulated response.

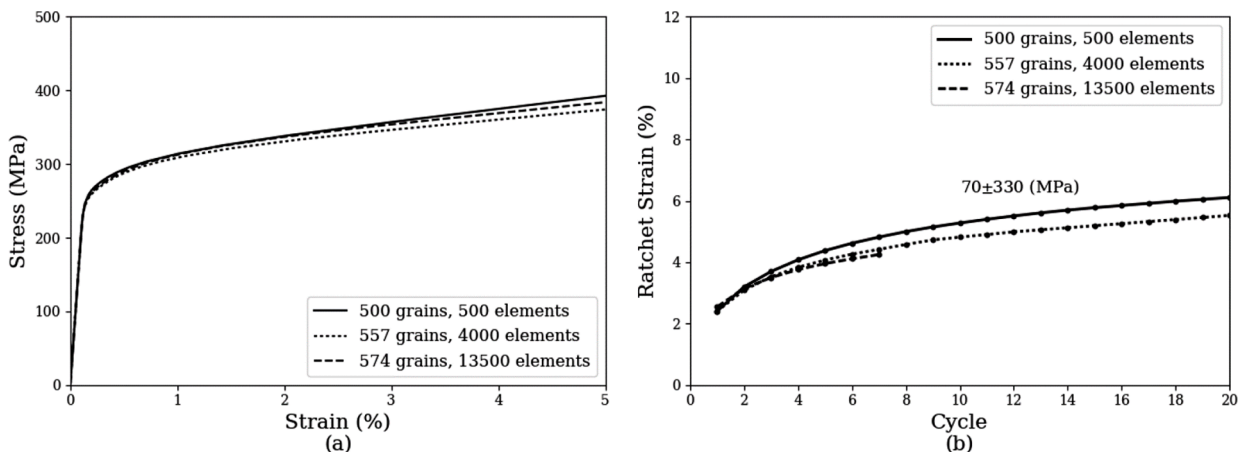
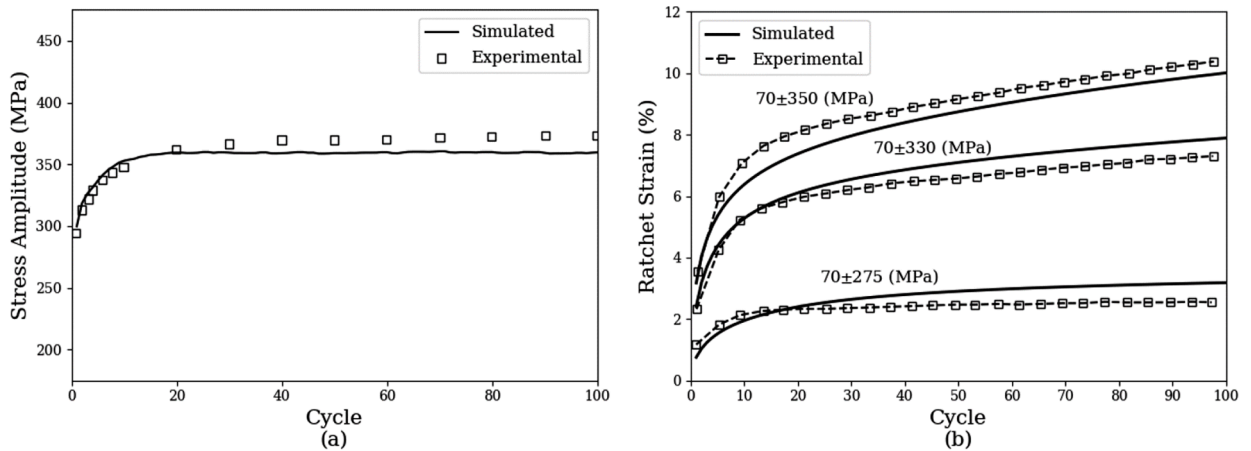


Fig. 19. Comparison of (a) stress-strain and (b) ratcheting responses as a function of mesh refinement. Ratchet strain response is mildly influenced by mesh refinement.

## Appendix C

While specific interest was placed on the material deformation transients that primarily occur within the first 50 cycles, the simulations shown in Fig. 11(a) and Fig. 12 were run for 100 cycles as a further demonstration of the proposed model framework. As can be seen in Fig. 20, relatively good agreement is maintained for up to 100 cycles.



**Fig. 20.** Plots showing material deformation response for up to 100 cycles. The loading parameters for (a) correspond to those used to generate Fig. 11, and the loading parameters for (b) correspond to those used to generate Fig. 12. Experimental data from Kang et al. (2011).

## References

- Abaqus, G., 2011. Abaqus 6.11. Dassault Systemes Simulia Corp Providence, RI, USA.
- Ahmed, J., Roberts, S.G., Wilkinson, A., 2006. Characterizing dislocation structure evolution during cyclic deformation using electron channelling contrast imaging. *Philosophical Magazine* 86, 4965–4981.
- Ananthakrishna, G., 2007. Current theoretical approaches to collective behavior of dislocations. *Physics Reports* 440, 113–259.
- Armstrong, P.J., Frederick, C., 1966. A mathematical representation of the multiaxial Bauschinger effect. Central Electricity Generating Board [and] Berkeley Nuclear Laboratories ....
- Armstrong, R., Rodriguez, P., 2006. Flow stress/strain rate/grain size coupling for fcc nanopolycrystals. *Philosophical Magazine* 86, 5787–5796.
- Arsenlis, A., Parks, D.M., 2002. Modeling the evolution of crystallographic dislocation density in crystal plasticity. *Journal of the Mechanics and Physics of Solids* 50, 1979–2009.
- Asaro, R.J., 1983. Crystal plasticity.
- Aslanides, A., Pontikis, V., 1998. Atomistic study of dislocation cores in aluminium and copper. *Computational materials science* 10, 401–405.
- Barrett, T.J., McCabe, R.J., Brown, D.W., Clausen, B., Vogel, S.C., Knezevic, M., 2020. Predicting deformation behavior of  $\alpha$ -uranium during tension, compression, load reversal, rolling, and sheet forming using elasto-plastic, multi-level crystal plasticity coupled with finite elements. *Journal of the Mechanics and Physics of Solids* 138, 103924.
- Bayerschen, E., McBride, A., Reddy, B., Böhlke, T., 2016. Review on slip transmission criteria in experiments and crystal plasticity models. *Journal of materials science* 51, 2243–2258.
- Berveiller, M., Zaoui, A., 1978. An extension of the self-consistent scheme to plastically-flowing polycrystals. *Journal of the Mechanics and Physics of Solids* 26, 325–344.
- Bonneville, J., Escaig, B., Martin, J., 1988. A study of cross-slip activation parameters in pure copper. *Acta Metallurgica* 36, 1989–2002.
- Brown, L., 2002. A dipole model for the cross-slip of screw dislocations in fcc metals. *Philosophical Magazine A* 82, 1691–1711.
- Castelluccio, G.M., Geller, C.B., McDowell, D.L., 2018. A rationale for modeling hydrogen effects on plastic deformation across scales in FCC metals. *International Journal of Plasticity* 111, 72–84.
- Castelluccio, G.M., McDowell, D.L., 2015. Microstructure and mesh sensitivities of mesoscale surrogate driving force measures for transgranular fatigue cracks in polycrystals. *Materials Science and Engineering: A* 639, 626–639.
- Castelluccio, G.M., McDowell, D.L., 2017. Mesoscale cyclic crystal plasticity with dislocation substructures. *International Journal of Plasticity* 98, 1–26.
- Chaboche, J.-L., 2008. A review of some plasticity and viscoplasticity constitutive theories. *International journal of plasticity* 24, 1642–1693.
- Chaboche, J., Van, K.D., Cordier, G., 1979. Modelization of the strain memory effect on the cyclic hardening of 316 stainless steel.
- Chandler, H., Bee, J., 1985. Cell structures in polycrystalline copper undergoing cyclic creep at room temperature. *Acta Metallurgica* 33, 1121–1127.
- Christodoulou, N., Woo, O.T., MacEwen, S.R., 1986. Effect of stress reversals on the work hardening behaviour of polycrystalline copper. *Acta Metallurgica* 34, 1553–1562.
- Clausen, B., Lorentzen, T., Leffers, T., 1998. Self-consistent modelling of the plastic deformation of f.c.c. polycrystals and its implications for diffraction measurements of internal stresses. *Acta Materialia* 46, 3087–3098.
- Coleman, B.D., Gurtin, M.E., 1967. Thermodynamics with internal state variables. *The journal of chemical physics* 47, 597–613.
- Conti, S., Ortiz, M., 2005. Dislocation microstructures and the effective behavior of single crystals. *Archive for Rational Mechanics and Analysis* 176, 103–147.
- Cottrell, A.H., 1953. *Dislocations and plastic flow in crystals*.
- Daymond, M., Bouchard, P., 2006. Elastoplastic deformation of 316 stainless steel under tensile loading at elevated temperatures. *Metallurgical and Materials transactions A* 37, 1863–1873.
- Devincere, B., Hoc, T., Kubin, L., 2008. Dislocation mean free paths and strain hardening of crystals. *Science* 320, 1745–1748.
- Devincere, B., Kubin, L., Hoc, T., 2006. Physical analyses of crystal plasticity by DD simulations. *Scripta Materialia* 54, 741–746.
- Devincere, B., Kubin, L., Hoc, T., 2007. Collinear superjogs and the low-stress response of fcc crystals. *Scripta Materialia* 57, 905–908.
- Dong, Y., He, X., Zhang, Z., 2020. A new crystal plasticity modeling of uniaxial ratcheting behavior for face-centered cubic 6061 aluminum alloy. *Materials Research Express* 7, 106515.

- Dong, Y., Kang, G., Yu, C., 2014. A dislocation-based cyclic polycrystalline visco-plastic constitutive model for ratchetting of metals with face-centered cubic crystal structure. *Computational materials science* 91, 75–82.
- El-Azab, A., 2000. The boundary value problem of dislocation dynamics. *Modelling and Simulation in Materials Science and Engineering* 8, 37.
- Eshelby, J.D., 1957. The determination of the elastic field of an ellipsoidal inclusion, and related problems. *Proceedings of the royal society of London. Series A. Mathematical and physical sciences* 241, 376–396.
- Essmann, U., Mughrabi, H., 1979. Annihilation of dislocations during tensile and cyclic deformation and limits of dislocation densities. *Philosophical Magazine* A 40, 731–756.
- Estrin, Y., Braasch, H., Brechet, Y., 1996. A dislocation density based constitutive model for cyclic deformation. *Journal of engineering materials and technology* 118, 57–70.
- Estrin, Y., Mecking, H., 1984. A unified phenomenological description of work hardening and creep based on one-parameter models. *Acta Metallurgica* 32, 57–70.
- Estrin, Y., Toth, L., Molinari, A., Bréchet, Y., 1998. A dislocation-based model for all hardening stages in large strain deformation. *Acta Materialia* 46, 5509–5522.
- Feaugas, X., 1999. On the origin of the tensile flow stress in the stainless steel AISI 316L at 300 K: back stress and effective stress. *Acta Materialia* 47, 3617–3632.
- Feltner, C., 1965. A debris mechanism of cyclic strain hardening for FCC metals. *Philosophical Magazine* 12, 1229–1248.
- Franciosi, P., Berveiller, M., Zaoui, A., 1980. Latent hardening in copper and aluminium single crystals. *Acta Metallurgica* 28, 273–283.
- Franciosi, P., Zaoui, A., 1982. Multislip in fcc crystals a theoretical approach compared with experimental data. *Acta Metallurgica* 30, 1627–1637.
- Gaudin, C., Feaugas, X., 2004. Cyclic creep process in AISI 316L stainless steel in terms of dislocation patterns and internal stresses. *Acta Materialia* 52, 3097–3110.
- Gaudin, C., Guillemer-Neel, C., Feaugas, X., 2001. Hardening rate under reverse loading in 316 L: Back stress and effective stress evolutions. *Journal de physique. IV* 11, 285–292.
- Gérard, C., Cailletaud, G., Bacroix, B., 2013. Modeling of latent hardening produced by complex loading paths in FCC alloys. *International journal of plasticity* 42, 194–212.
- Gorlier, C., 1984. Mécanismes de fatigue plastique de l'acier 316L sous formes monocristalline et polycristalline. Ecole des Mines de St-Etienne. Thèse de doctorat.
- Grober, M.A., Jackson, M.A., 2014. DREAM.3D: A Digital Representation Environment for the Analysis of Microstructure in 3D. *Integrating Materials and Manufacturing Innovation* 3, 56–72.
- Hansen, B., Bronkhorst, C., Ortiz, M., 2010. Dislocation subgrain structures and modeling the plastic hardening of metallic single crystals. *Modelling and Simulation in Materials Science and Engineering* 18, 055001.
- Hasegawa, T., Yakou, T., Karashima, S., 1975. Deformation behaviour and dislocation structures upon stress reversal in polycrystalline aluminium. *Materials Science and Engineering* 20, 267–276.
- Hasegawa, T., Yakou, T., Kocks, U., 1986. Forward and reverse rearrangements of dislocations in tangled walls. *Materials Science and Engineering* 81, 189–199.
- Hershey, A., 1954. The elasticity of an isotropic aggregate of anisotropic cubic crystals. *Journal of Applied mechanics-transactions of the ASME* 21, 236–240.
- Hill, R., 1965. Continuum micro-mechanics of elastoplastic polycrystals. *Journal of the Mechanics and Physics of Solids* 13, 89–101.
- Hutchinson, J., 1970. Elastic-plastic behaviour of polycrystalline metals and composites. *Proceedings of the Royal Society of London. A. Mathematical and Physical Sciences* 319, 247–272.
- Jiang, Y., Sehitoglu, H., 1996. Modeling of cyclic ratchetting plasticity, part I: development of constitutive relations.
- Kang, G., Dong, Y., Wang, H., Liu, Y., Cheng, X., 2010. Dislocation evolution in 316L stainless steel subjected to uniaxial ratchetting deformation. *Materials Science and Engineering: A* 527, 5952–5961.
- Kang, G., Liu, Y., Dong, Y., Gao, Q., 2011. Uniaxial Ratchetting Behaviors of Metals with Different Crystal Structures or Values of Fault Energy: Macroscopic Experiments. *Journal of Materials Science & Technology* 27, 453–459.
- Karaman, I., Sehitoglu, H., Maier, H., Chumlyakov, Y., 2001. Competing mechanisms and modeling of deformation in austenitic stainless steel single crystals with and without nitrogen. *Acta Materialia* 49, 3919–3933.
- Kayali, E.S., Plumtree, A., 1982. Stress-substructure relationships in cyclically and monotonically deformed wavy slip mode metals. *Metallurgical Transactions A* 13, 1033–1041.
- Khadyko, M., Dumoulin, S., Cailletaud, G., Hopperstad, O.S., 2016. Latent hardening and plastic anisotropy evolution in AA6060 aluminium alloy. *International Journal of Plasticity* 76, 51–74.
- Khan, A.S., Huang, S., 1995. *Continuum theory of plasticity*. John Wiley & Sons.
- Kitayama, K., Tomé, C., Rauch, E., Gracio, J., Barlat, F., 2013. A crystallographic dislocation model for describing hardening of polycrystals during strain path changes. Application to low carbon steels. *International Journal of Plasticity* 46, 54–69.
- Kocks, U., 1966. A statistical theory of flow stress and work-hardening. *Philosophical Magazine* 13, 541–566.
- Kocks, U., Franciosi, P., Kawai, M., 1991. A forest model of latent hardening and its application to polycrystal deformations. *Textures and microstructures* 14, 1103–1114.
- Kocks, U., Mecking, H., 2003. Physics and phenomenology of strain hardening: the FCC case. *Progress in materials science* 48, 171–273.
- Kocks, U.F., AS, A., MF, A., 1975. *Thermodynamics and kinetics of slip*.
- Korsunsky, A.M., Hofmann, F., Song, X., Eve, S., Collins, S.P., 2010. Probing deformation substructure by synchrotron x-ray diffraction and dislocation dynamics modelling. *Journal of nanoscience and nanotechnology* 10, 5935–5950.
- Kubin, L., Devincere, B., Hoc, T., 2008. Modeling dislocation storage rates and mean free paths in face-centered cubic crystals. *Acta materialia* 56, 6040–6049.
- Kubin, L.P., Canova, G., Condat, M., Devincere, B., Pontikis, V., Bréchet, Y., 1992. Dislocation microstructures and plastic flow: a 3D simulation. *Solid State Phenomena. Trans Tech Publ* 455–472.
- Kuhlmann-Wilsdorf, D., 1962. A new theory of work hardening in crystals. PENNSYLVANIA UNIV, PHILADELPHIA.
- Kuhlmann-Wilsdorf, D., Comins, N., 1983. Dislocation cell formation and work hardening in the unidirectional glide of fcc metals I: Basic theoretical analysis of cell walls parallel to the primary glide plane in early stage II. *Materials Science and Engineering* 60, 7–24.
- Laird, C., Charsley, P., Mughrabi, H., 1986. Low energy dislocation structures produced by cyclic deformation. *Materials science and engineering* 81, 433–450.
- Langer, J., Bouchbinder, E., Lookman, T., 2010. Thermodynamic theory of dislocation-mediated plasticity. *Acta Materialia* 58, 3718–3732.
- Lukáš, P., Klesnil, M., Krejčí, J., 1968. Dislocations and persistent slip bands in copper single crystals fatigued at low stress amplitude. *physica status solidi (b)* 27, 545–558.
- Lukáš, P., Kunz, L., Svoboda, M., 1999. Stress-strain response and fatigue life of copper single crystals cyclically loaded with a positive mean stress. *Materials Science and Engineering: A* 272, 31–37.
- Madeo, R., Devincere, B., Kubin, L., Hoc, T., Rodney, D., 2003. The role of collinear interaction in dislocation-induced hardening. *Science* 301, 1879–1882.
- Madeo, R., Devincere, B., Kubin, L.P., 2002. From dislocation junctions to forest hardening. *Physical review letters* 89, 255508.
- Marukawa, K., Sanpei, T., 1971. Stability of the work hardened state against stress reversal in copper single crystals. *Acta Metallurgica* 19, 1169–1176.
- McDowell, D., 1995. Stress state dependence of cyclic ratchetting behavior of two rail steels. *International Journal of Plasticity* 11, 397–421.
- McDowell, D.L., 2008. Viscoplasticity of heterogeneous metallic materials. *Materials Science and Engineering: R: Reports* 62, 67–123.
- Mecking, H., Kocks, U., 1981. Kinetics of flow and strain-hardening. *Acta metallurgica* 29, 1865–1875.
- Milligan, R., Koo, W., Davidson, T., 1966. The Bauschinger effect in a high-strength steel.
- Moosbrugger, J., McDowell, D., 1989. On a class of kinematic hardening rules for nonproportional cyclic plasticity.
- Mughrabi, H., 1979. Microscopic mechanisms of metal fatigue, *Strength of metals and alloys*. Elsevier, pp. 1615–1638.
- Mughrabi, H., 1983. Dislocation wall and cell structures and long-range internal stresses in deformed metal crystals. *Acta metallurgica* 31, 1367–1379.
- Mughrabi, H., 1987a. The long-range internal stress field in the dislocation wall structure of persistent slip bands. *physica status solidi (a)* 104, 107–120.
- Mughrabi, H., 1987b. A two-parameter description of heterogeneous dislocation distributions in deformed metal crystals. *Materials science and engineering* 85, 15–31.
- Mughrabi, H., Pschenitzka, F., 2005. Constrained glide and interaction of bowed-out screw dislocations in confined channels. *Philosophical Magazine* 85, 3029–3045.
- Mura, T., 2013. *Micromechanics of defects in solids*. Springer Science & Business Media.

- Nabarro, F.R., Duesbery, M.S., 2002. Dislocations in solids. Elsevier.
- Ohno, N., Wang, J.-D., 1993. Kinematic hardening rules with critical state of dynamic recovery, part I: formulation and basic features for ratchetting behavior. *International journal of plasticity* 9, 375–390.
- Orowan, E., 1959. Internal stresses and fatigue in metals. GM Rassweiler and WL Grube eds, p. 59.
- Oudriss, A., Feaugas, X., 2016. Length scales and scaling laws for dislocation cells developed during monotonic deformation of (001) nickel single crystal. *International Journal of Plasticity* 78, 187–202.
- Patra, A., McDowell, D.L., 2012. Crystal plasticity-based constitutive modelling of irradiated bcc structures. *Philosophical Magazine* 92, 861–887.
- Pham, M., Holdsworth, S., Janssens, K., Mazza, E., 2013. Cyclic deformation response of AISI 316L at room temperature: mechanical behaviour, microstructural evolution, physically-based evolutionary constitutive modelling. *International Journal of Plasticity* 47, 143–164.
- Polak, J., 1991. Cyclic plasticity and low cycle fatigue life of metals. Elsevier, Amsterdam.
- Prager, W., 1956. A new methods of analyzing stresses and strains in work hardening plastic solids. *J. Appl. Mech.(ASME)* 23, 493–496.
- Rao, S., Parthasarathy, T., Woodward, C., 1999. Atomistic simulation of cross-slip processes in model fcc structures. *Philosophical Magazine A* 79, 1167–1192.
- Rasmussen, T., Vegge, Leffers, T., Pedersen, O., Jacobsen, K.W., 2000. Simulation of structure and annihilation of screw dislocation dipoles. *Philosophical Magazine A* 80, 1273–1290.
- Ren, X., Yang, S., Wen, G., Zhao, W., 2020. A Crystal-Plasticity Cyclic Constitutive Model for the Ratchetting of Polycrystalline Material Considering Dislocation Substructures. *Acta Mechanica Solida Sinica* 33, 268–280.
- Roberts, J., Barnett, D., 1965. Nonelastic strain recovery of copper single crystals after small prestrains. *Acta Metallurgica* 13, 1027–1029.
- Salama, K., Roberts, J.M., 1970. Back recovery microstrains in stage II deformation of copper. *Scripta Metallurgica* 4, 749–754.
- Sauzay, M., 2008. Analytical modelling of intragranular backstresses due to deformation induced dislocation microstructures. *International Journal of Plasticity* 24, 727–745.
- Sauzay, M., Kubin, L.P., 2011. Scaling laws for dislocation microstructures in monotonic and cyclic deformation of fcc metals. *Progress in Materials Science* 56, 725–784.
- Sauzay, M., Liu, J., Rachdi, F., Signor, L., Ghidossi, T., Villechaise, P., 2014. Physically-based simulations of the cyclic behavior of FCC polycrystals. *Advanced Materials Research. Trans Tech Publ* 833–839.
- Schwartz, J., Fandeur, O., Rey, C., 2013. Numerical approach of cyclic behaviour of 316LN stainless steel based on a polycrystal modelling including strain gradients. *International journal of fatigue* 55, 202–212.
- Steckmeyer, A., Sauzay, M., Weidner, A., Hieckmann, E., 2012. Micromechanical modelling of the cyclic stress–strain behaviour of nickel polycrystals. *International Journal of Fatigue* 40, 154–167.
- Taylor, G.I., 1934. The mechanism of plastic deformation of crystals. Part I.—Theoretical. *Proceedings of the Royal Society of London. Series A, Containing Papers of a Mathematical and Physical Character* 145, 362–387.
- Tippelt, B., Breitschneider, J., Hähner, P., 1997. The dislocation microstructure of cyclically deformed nickel single crystals at different temperatures. *physica status solidi (a)* 163, 11–26.
- Verdier, M., Fivel, M., Groma, I., 1998. Mesoscopic scale simulation of dislocation dynamics in fcc metals: Principles and applications. *Modelling and Simulation in Materials Science and Engineering* 6, 755.
- Wang, Z., Beyerlein, I., LeSar, R., 2007. The importance of cross-slip in high-rate deformation. *Modelling and simulation in materials science and engineering* 15, 675.
- Wang, Z., Gong, B., Wang, Z., 1997. Cyclic deformation behavior and dislocation structures of [001]copper single crystals—II. Characteristics of dislocation structures. *Acta materialia* 45, 1379–1391.
- Wen, W., Borodachenkova, M., Tomé, C., Vincze, G., Rauch, E., Barlat, F., Grácio, J., 2016. Mechanical behavior of low carbon steel subjected to strain path changes: Experiments and modeling. *Acta Materialia* 111, 305–314.
- Xia, S., Belak, J., El-Azab, A., 2016. The discrete-continuum connection in dislocation dynamics: I. Time coarse graining of cross slip. *Modelling and Simulation in Materials Science and Engineering* 24, 075007.
- Zecevic, M., Knezevic, M., 2015. A dislocation density based elasto-plastic self-consistent model for the prediction of cyclic deformation: Application to AA6022-T4. *International Journal of Plasticity* 72, 200–217.
- Zhou, C., Biner, S.B., LeSar, R., 2010. Discrete dislocation dynamics simulations of plasticity at small scales. *Acta Materialia* 58, 1565–1577.
- Zhou, Z., Zhu, Y., Luo, J., Yang, X., Guo, X., 2020. Characterisation of dislocation patterning behaviour with a continuum dislocation dynamics model on two parallel slip planes equipped with a deep neural network resolving local microstructures. *International Journal of Solids and Structures* 198, 57–71.